AN ABSTRACT OF THE THESIS OF

Kyle Gulan for the degree of Master of Science in Electrical and Computer Engineering presented on May 29, 2019.

Title: Charging Analysis of Ground Support Vehicles in an Electrified Airport

Abstract approved: ____

Eduardo Cotilla-Sanchez Yue Cao

While electrification is currently one of the largest trends in the automotive world, other related industries are also evaluating electrification opportunities as a means to reduce environmental impact, emissions, and noise pollution. One such sector is the aviation industry. While it is generally accepted that all-electric aircraft are not a realization in the most immediate future, there are still large sections of the airport that can undergo electrification. The quickest path to an electrified airport is starting with the ground support vehicles. To accomplish the goal of eliminating traditional fossil fuel vehicles, two key criteria must be met: intelligent scheduling and efficient charging. This Thesis seeks to accomplish both by first proposing a scheduling scheme that can help an electrified airport choose which vehicles are required while at the same time intelligently charging unused vehicles. Second, we perform a component level analysis on a purpose built off-board vehicle charger designed for use on ground support vehicles in an electrified airport.

Charging Analysis of Ground Support Vehicles in an Electrified Airport

by

Kyle Gulan

A THESIS

submitted to

Oregon State University

in partial fulfillment of
the requirements for the
degree of

Master of Science

Presented May 29, 2019
Commencement June 2019

Master of Science thesis of Kyle Gulan presented on May 29, 2019.

APPROVED:

Co-Major Professor, representing Electrical and Computer Engineering

---

Co-Major Professor, representing Electrical and Computer Engineering

---

Head of the School of Electrical Engineering and Computer Science

---

Dean of the Graduate School

I understand that my thesis will become part of the permanent collection of Oregon State University libraries. My signature below authorizes release of my thesis to any reader upon request.

Kyle Gulan, Author

ACKNOWLEDGEMENTS

I would like to acknowledge all of my family, friends, past teachers, coworkers, and anybody who has helped me get where I am today. I couldn't have done it without each of you.

I would also like to particularly thank Dr. Eduardo Cotilla-Sanchez for taking me in and making me feel at home when I was unsure of where my graduate schooling might take me. I would also like to thank Dr. Yue Cao for his help during my second year in writing my published conference paper as well as his help with my component level analysis.

Finally, I would like to thank my parents. Without your support for the past 6 years, this never would have been possible.

TABLE OF CONTENTS

Page

1 Introduction . . . 1

2 Charging Analysis of Ground Support Vehicles in an Electrified Airport . 3
- 2.1 Introduction . . . 3
- 2.2 Electrified Airport Model . . . 4
- 2.3 Simulation of an Electrified Airport . . . 9
- 2.4 Results and Analysis . . . 12
- 2.5 Conclusion . . . 19

3 Analysis of a Purpose Built Charger for Ground Support Vehicles in an Electrified Airport . . . 21
- 3.1 Introduction . . . 21
- 3.2 Background . . . 22
- 3.3 Proposed Charger . . . 31
  - 3.3.1 Charging . . . 31
  - 3.3.2 Vehicle-to-Grid . . . 37
  - 3.3.3 Components . . . 39
- 3.4 Charging Results . . . 53
- 3.5 Vehicle to Grid Results . . . 65
- 3.6 Future Work and Conclusion . . . 77

4 Conclusion . . . 81

Appendices . . . 89
- A PLECS Blockset . . . 90

LIST OF FIGURES

Figure | Page

2.1 Sample airport baseline load with random noise 5

2.2 Flowchart of the simulation algorithm. 11

2.3 Total cost of vehicles versus gallons of gas used for parameters set in Table 1. A Pareto Front reference is shown in red. 15

2.4 Total cost of vehicles versus gallons of gas used versus number of Class A vehicles for the parameters set in Table 2.2. 16

2.5 Total cost of vehicles versus gallons of gas used versus number of chargers for the parameters set in Table 2.2. 18

2.6 Total cost of vehicles versus gallons of gas used versus SOC weight and color coded by Availability weights 19

3.1 Typical on-board battery charger schematic [20] 23

3.2 Inductor current in a sample system using boost PFC 25

3.3 Input current of a sample system without and with boost PFC . . . 26

3.4 Comparator, switching, and output waveforms for an inverter using bipolar switching techniques [21] 29

3.5 Comparator, switching, and output waveforms for an inverter using unipolar switching techniques [21] 30

3.6 Proposed battery charger divided into sections 32

3.7 PFC stage operation during the positive half cycle of the AC waveform [26] 33

3.8 PFC stage operation during the negative half cycle of the AC waveform [26] 34

3.9 Totem pole PFC cascaded controllers 35

3.10 Battery model used to simulate a vehicle battery 37

3.11 MOSFET turn on waveforms [34] 46

3.12 Duty cycle of the non boost MOSFET as calculated within PLECS 49

LIST OF FIGURES (Continued)

Figure Page

3.13 Heat sink and buck or boost MOSFET junction temperature while charging a 350 V vehicle at 20 A 52

3.14 Battery voltage and current for the charging of the 350 V vehicle . 54

3.15 Transient and ripple of battery voltage and current for the charging of the 350 V vehicle 55

3.16 Grid voltage and current for the charging of the 350 V vehicle . . . 57

3.17 Current ripple of the inductor within the buck stage while charging a 350 V vehicle 58

3.18 Current ripple of the inductor within the PFC stage while charging a 350 V vehicle 59

3.19 Battery voltage and current while charging a 96 V vehicle 60

3.20 Grid voltage and current to the charger while charging a 96 V vehicle 61

3.21 Battery voltage and current to the battery while charging a 48 V vehicle 62

3.22 Grid voltage and current to the charger while charging a 48 V vehicle 63

3.23 Voltage over the DC link capacitor while charging a 48 V vehicle . . 64

3.24 Voltage over the battery capacitor while charging a 48 V vehicle . . 65

3.25 Voltage, current, and power being sent to the grid from the 350 V vehicle in V2G mode 67

3.26 Voltage and current from the 350 V vehicle in V2G mode 68

3.27 Voltage of the DC link capacitor during V2G mode while a 350 V vehicle is plugged in 69

3.28 Voltage, current, and power being sent to the grid from the 96 V vehicle in V2G mode 70

3.29 Voltage and current from the battery of the 96 V vehicle in V2G mode 71

LIST OF FIGURES (Continued)

Figure Page

3.30 Voltage, current, and power being sent to the grid from the 48 V vehicle in V2G mode 73

3.31 Voltage and current from the battery of the 48 V vehicle in V2G mode 74

3.32 Grid voltage and current to the charger while in charging mode with emphasis on the inrush current 75

3.33 Grid voltage and current to the charger while in charging mode with a reduced DC link capacitor value with emphasis on the inrush current 76

3.34 DC link capacitor voltage with a reduced DC link capacitor value . 77

LIST OF TABLES

Table Page

2.1 Number of required vehicles to service each plane entering the terminal 7

2.2 Parameters used for vehicle charging simulation 14

3.1 Design goals of the off-board battery charger 40

3.2 Specifications of various batteries to be charged using the proposed charger 41

3.3 Attributes of chosen MOSFETs 47

3.4 Power losses of switching components 50

LIST OF APPENDIX FIGURES

Figure | Page

A.1 The proposed charger model as seen in PLECS 91

A.2 PFC controls for vehicle charging as seen in PLECS 92

A.3 V2G controls as seen in PLECS 93

A.4 Buck/boost stage controls as seen in PLECS 94

Chapter 1: Introduction

In today's transportation world, electrification is one of the key topics under very active discussion and development. Many industries including aviation are interested in expanding into this area of electrified transportation. While a significant push is being made towards developing more or all-electric aircraft, the technology is still under development. Another venue whereby an airport could become more electrified is in the ground support vehicles. These vehicles service the planes by way of bringing food, water, and passengers to the plane. They also are able to move planes around as well as hauling and loading luggage or cargo.

Because most of the vehicles that currently perform these tasks are fossil fuel vehicles, changing to electric vehicles would present a number of challenges particularly with strategizing their charging periods in a highly challenging environment. With fossil fuel vehicles, gas or other fuel source only needs to be added to the tank and after a few minutes, the vehicle is ready to run again. In the case of electric vehicles, many times they require hours to fully recharge. This necessitates a scheduling system that both intelligently uses and charges the vehicles to ensure that there are enough vehicles to complete the jobs required of them.

Not only do these vehicles need to be charged intelligently, they need to be charged efficiently. Rather than use an already existing product, a purpose built charger that can meet the unique needs of the electrified airport should be created.

This charger ensures that all functions required by the airport are met. This includes being mounted off-board, able to charge different types of vehicles and being bidirectional for vehicle-to-grid operation while at the same time, remaining efficient.

This paper contains two manuscripts. Each will contain relevant background and justification for the exercises performed within it. One will describe how ground support vehicles within an electrified airport can be intelligently be scheduled. It will also describe how an airport could optimize the amount of electric vehicles it requires so as to limit the amount of gas vehicles required when the electric ones could not completely complete the tasks needed. The second manuscript proposes a purpose built charger that will meet all the requirements of a battery charger within an electrified airport. The paper will end with the final thoughts and future work for each paper.

Chapter 2: Charging Analysis of Ground Support Vehicles in an Electrified Airport

2.1 Introduction

With automotive electrification becoming a reality, the aviation industry is also making strides into more or all electric aircraft [1, 2]. While all electric aircraft may not be in the near future, a prerequisite of such innovation is electrified airport infrastructure [3]. All major airports currently have a set of ground support vehicles on the airside, which interact with the planes as they complete their flying and servicing cycles. Most of these existing vehicles are gasoline or diesel vehicles. Changing these fossil fuel vehicles to plug-in electric vehicles is a key way in which an airport moves towards electrification.

As a fully electrified fleet of ground support vehicles is realized, a number of challenges arise. The biggest challenge pertains to the significantly longer charging time compared to refueling conventional fossil-fueled vehicles. Another central issue involves the increased burden on the electric grid, including both rises in steady-state loads and dynamic disturbances.

Overcoming the extended charging time and minimizing the load on grid components requires thorough system planning and sufficient backup vehicles [4]. To optimize the system, the ground support vehicles must be charged under intelligent scheduling based on variable pricing and required airplane support at peak and off-peak times. A smart scheduling system of charging, similar to one used with fleets of on-road vehicles, is required due to the large number of vehicles in service. This system can benefit from reduced off-hour electricity rates while putting less strain on physical components of the grid and ensuring its stability [5, 6, 7, 8, 9].

This paper designs a system that addresses the above issues, using a synthesized model of one terminal at a medium to large-sized international airport. A Monte Carlo simulation along with the Pareto front analysis will show the effect of various factors on the systems performance as well as the efficacy of an optimization algorithm. At the end of the paper we present the overall conclusions and closing arguments.

2.2 Electrified Airport Model

The proposed electrified airport model consists of the general electrical load of the airport, the ground support vehicles and the vehicle chargers where their use is governed by a scheduling algorithm to determine usage and charging times. This charging algorithm is designed to minimize the total number of electric vehicles required and the amount of gas vehicles used if electric vehicles are unavailable. The adjustable parameters of this model include the number of each type of ground support vehicle, number of chargers, charging algorithm weights, and maximum target load of the facility.

In addition, the system has a number of other variables that are not adjustable but are factors that affect system performance. The largest factor is the base load of the airport. This includes any other electrical load on the property that is not vehicles charging such as lighting and heating. The charging algorithm will keep the total electrical load of the facility at or below the max target load. A sample of the airport load with random noise is shown in Figure 2.1. The number of planes entering the terminal is determined randomly according to a uniform random distribution. During peak hours, an exponential random distribution is also summed to simulate potentially higher traffic.

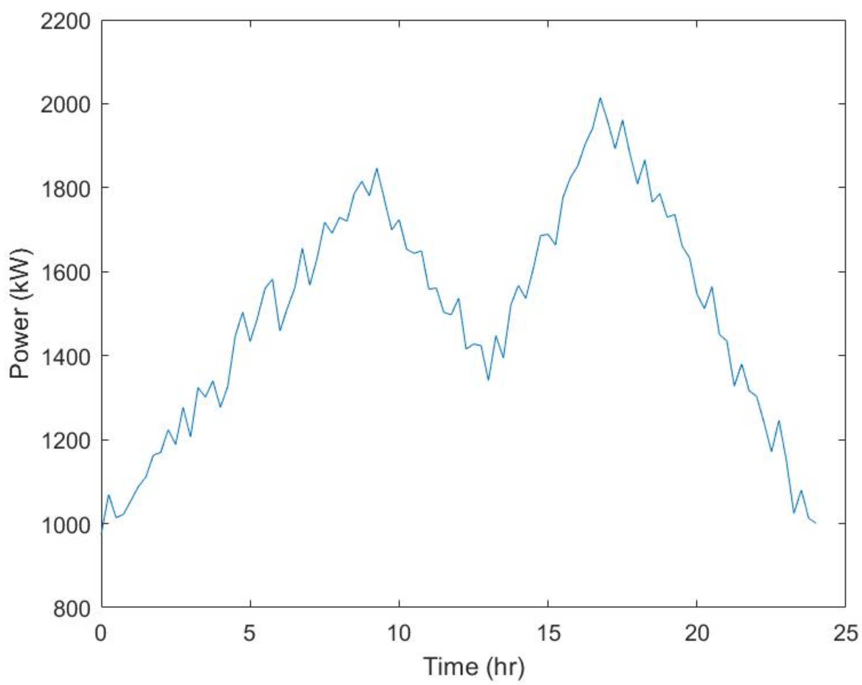

Figure 2.1: Sample airport baseline load with random noise

The ground support vehicles are split into three categories: A, B, and C. Class

A vehicles are typical on-road vehicles. These vehicles are used to transport fuel, food, deicing fluid, and people around the airport property. Class B vehicles are high-powered tug tractors that are responsible for pushing the plane back from the gate. Class C vehicles are small, low power tug tractors that handle cargo.

Every vehicle in the system has a number of attributes in the "vehicle matrix" which includes the vehicles' state of charge (SOC), availability, current activity, vehicle type and tag number. The SOC is initially set randomly by a random uniform distribution. Availability is calculated for an entire class of vehicles and is defined by the number of vehicles that could be used to immediately service planes divided by the total number of vehicles in that specific class. For each time step, each vehicle is ranked and then reordered according to the attributes within the vehicle matrix. Vehicles with low SOC and availability have high ranks and thus have charger priority over other vehicles. The ranking function is defined as

$$Rank = (1 - SOC) \cdot W_{SOC} + (1 - A) \cdot W_{\text{Avail}} \tag{2.1}$$

where W is the charging weights, and A represents the availability:

$$A = \frac{\text{Class X Vehicles with SOC>0.5}}{\text{Total Vehicles in Class X}}. \tag{2.2}$$

This method of ranking each vehicle forces the algorithm to give vehicles with low SOC and availability precedence over vehicles that are closer to fully charged as well as having similar vehicles ready to be used.

The number of planes coming in at the given time step determines how many of each vehicle class are required. When there are not enough electric vehicles available at a time step to cover all the required jobs, gas vehicles are used. The number of vehicles required per plane is shown in Table 2.1. The number of gas vehicles required at the given time step is the difference of the required number of vehicles minus the amount of available vehicles according to (2.3) where $N_{\text{gas},X}$ is the number of gas vehicles used in a given class, $N_{\text{elec,required},X}$ is the number of required electric vehicles in a given class per plane, and P represents the number of planes at the time step.

Table 2.1: Number of required vehicles to service each plane entering the terminal

Vehicle Class	A	B	C
Number of Vehicles Required	3 (5)	1	3

Class A vehicles have the added constraint that if five or more planes enter the terminal at the same time, five class A vehicles are required to account for the potential of having to move people to the terminal if there are no open gates at the time.

$$N_{\text{gas},X} = (N_{\text{elec},X,\text{required}} \cdot P) - N_{\text{elec,avail}} \tag{2.3}$$

The algorithm then checks how many vehicles can charge by dividing the difference of the max electrical load and current airport load by the load one vehicle charging would require. This is shown according to (2.4) where $N_{\text{charge,max}}$ is defined as the maximum number of vehicles that can charge at the time step and $Load_{\text{charge,1 vehicle}}$ is defined as the amount of power required to charge the vehicle during the time step.

$$N_{\text{charge,max}} = \frac{Load_{\text{max}} - Load(t)}{Load_{\text{charge,1 vehicle}}} \tag{2.4}$$

Finally, the SOC of each vehicle in service is updated. If the vehicle is charging, the SOC increases by the amount of energy the charger provides it during the time step in terms of SOC. This is shown in (2.5). If the vehicle is servicing a plane, the SOC decreases by the amount of energy expelled to complete the task in terms of SOC as shown by (2.6).

$$SOC_{\text{final}} = SOC_{\text{initial}} + SOC_{\text{charge}} \tag{2.5}$$

$$SOC_{\text{final}} = SOC_{\text{initial}} - SOC_{\text{service}} \tag{2.6}$$

If the SOC of a vehicle is charged and surpasses 100%, the amount of energy added to the vehicle is averaged over the time step and the overage is subtracted from the charge rate. The SOC is then set to 100% and the vehicle will no longer charge.

Once the time step is complete, the model moves to the next time step and repeats the process for the remaining time steps. Each set of parameters is run for three separate days each with random inputs that are consistent between each varying set of parameters. In the end, the total amount of gas used is calculated by equating the electrical energy that would have been used if electric vehicles were available to amount of energy within gasoline and averaged over the 3 days that are simulated.

2.3 Simulation of an Electrified Airport

A Monte Carlo simulation estimates a solution to a problem by running many trials of a system that contains one or more random variables. By running many trials, the law of large numbers states that the average output of the simulation is a close approximation to the actual solution. We chose this type of simulation due to the stochastic nature of the inputs such as initial values in the vehicle matrix and the number of planes at any given time. A Monte Carlo simulation is also used because the model contains a large number of adjustable parameters that can significantly affect the results [10]. In this specific case, the Monte Carlo simulation allows the user to run many trials while changing the various parameters and analyzing how the system is affected by the changes between each trial.

The concept of the Pareto front is used to analyze the results of the Monte Carlo simulation and find any optima. The Pareto front is defined when no more design variables can be optimized without negatively influencing another variable of interest [11]. A simplified way to visualize the Pareto front is plotting simulation results as points, then the Pareto front is a cluster of multiple data points nearest to the ideal combination of design variables. The Pareto front is useful when there is not one clear solution, but when there are a large amount of data points in a multi-variable optimization problem such as a Monte Carlo simulation of an electrified airport. In the case of the electric airport, the design goal is to spend the least amount of money on vehicles while also using the least amount of gas.

The Monte Carlo simulation is implemented in MATLAB code and has three main sections: initialization, time-step iterations, and output plotting. The constants of the simulation are set in the initialization section, which includes maximum and minimum number of vehicles and chargers, charge rates, battery data, and airport base electrical load.

The electrified airport model is implemented in the iterative stage. Here, the parameters are determined and inputted into a set of time step loops that simulate a day of operation. Each time step is defined as 15 minutes. The days are run multiple times with preset random values and attributes to ensure that the average of the random numbers guiding the system are as close to the true expected value as possible. Once the set number of days is run, the parameters change, and the days are run again. A flowchart of this algorithm can be seen in Figure 2.2.

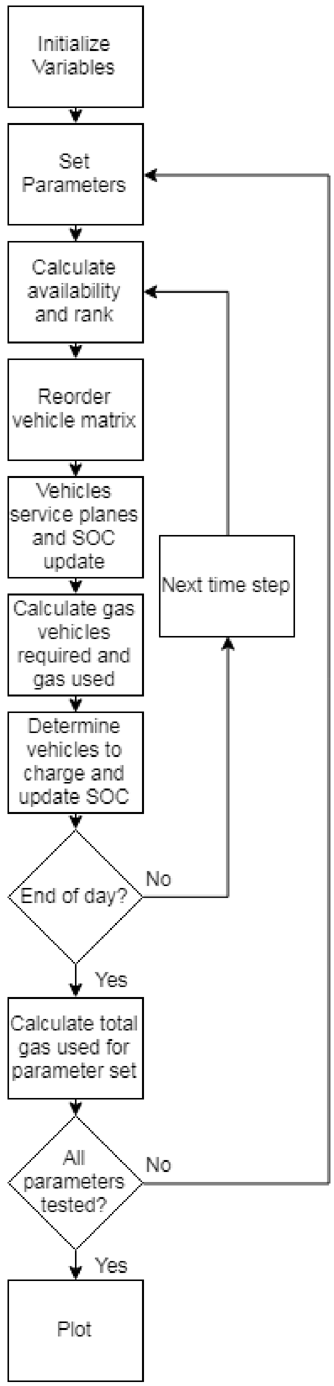

Figure 2.2: Flowchart of the simulation algorithm.

Once all the trials are run, relevant figures are created that focus on the analysis of the system.

2.4 Results and Analysis

In order to run the optimization analysis for the synthesized system, we impose a set of constraints on the system. These constraints drive the system to meet the design goal of controlling the overall electrical load of the facility as well as minimizing the overall cost of the system.

$$L_{\text{chargers}} + L_{\text{base}} < L_{\text{max}} \tag{2.7}$$

$$min[C] = f(N_A, N_B, N_C) \tag{2.8}$$

such that when

$$N_{X,\text{avail}}(t) < N_{X,\text{required}}(t) \tag{2.9}$$

the number of gas vehicles $N_{X,gas}$ is

$$N_{X,\text{gas}}(t) = N_{X,\text{required}}(t) - N_{X,\text{avail}}(t) \tag{2.10}$$

where L is defined as the electrical load of the airport, C is the total cost of the system and is a function of the amount of vehicles in each class and $N_X(t)$ is the number of vehicles at a given time step.

Equation (2.7) requires that the system only use up to the max power. This forces the system to charge more vehicles during off periods of the day while at the same time, avoiding excessive power spikes when the load is high.

Equation (2.8) defines the design goal of minimizing the cost of the system in the form of the number of vehicles purchased. It is supported by equations (2.9) and (2.10), which state that when there are not enough electric vehicles to fulfill the required duties, gas vehicles would be used in their place. From this, the amount of gas used per simulation and revolving set of parameters is calculated.

As previously mentioned, the Monte Carlo simulation is run with a range of parameters. As the simulation is running, the amount of gas is calculated by

$$G = \sum_{A,B,C} \frac{N_{X,\text{gas}} \cdot SOC_{\text{used}} \cdot \text{Capacity}_X \cdot 3.6}{E_{\text{spec}} \cdot 3.7854} \tag{2.11}$$

where G is defined as gallons of gas, $N_{X,\text{gas}}$ is the number of gas vehicles of class X, SOC_{used} is the amount of electrical energy required to complete the task, and E_{spec} is the specific energy per liter of automotive gas. The constant 3.6 converts from kW-hr to MJ and 3.7854 converts from liters to gallons.

In addition, Class A vehicles are set at \$60,000, Class B vehicles are set at \$40,000, and Class C vehicles are set at \$20,000. These prices reflect the average price of a small to medium size vehicle in each class [12, 13]. The total cost is calculated by

$$C = \sum_{A,B,C} N_X \cdot c_X \tag{2.12}$$

where C is the total cost of the vehicles, N_X is the number of vehicles in each class and c_X is the cost of a single vehicle in a given class.

A sample case study is proposed using the parameters shown in Table 2.2. Each parameter is set to have a range of values. All parameters begin at the initial value and increment up by delta until it reaches the max. Every unique combination of the various parameters is tested which allows for the most ideal solution within the set ranges to be seen.

Figure 2.3 shows the total amount of gas used versus the cost for the vehicles required. Within this plot, one can see the Pareto front in red. A clear example of a segment of this front is the set of data close to the point where less gas cannot be used without additional cost. This curve forms nearest to the point (0,0).

Table 2.2: Parameters used for vehicle charging simulation

Parameter	Initial	Delta	Final
Class A Vehicles	1	5	36
Class B Vehicles	1	2	9
Class C Vehicles	1	5	36
Chargers	25	5	45
SOC Weight	1	2	9
Availability Weight	1	2	9

Multidimensional graphs can be created to show and optimize how many vehicles are being used. Figure 2.4 shows a plot of the same data presented previously coupled with the number of Class A vehicles. From this plot, the minimum num-

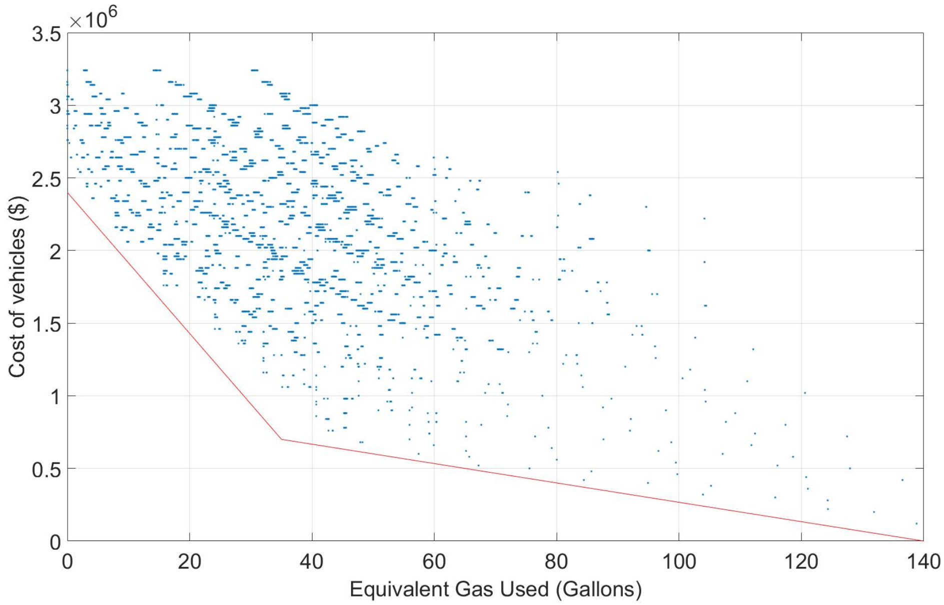

Figure 2.3: Total cost of vehicles versus gallons of gas used for parameters set in Table 1. A Pareto Front reference is shown in red.

ber of Class A vehicles required to achieve zero gas usage can be found. For each number of Class A vehicles within its range, every other combination of parameters has been tested with it. Thus, if no points on a level reach the y-axis (0 gallons of gas used), there is no solution that uses that number of Class A vehicles within the bounds of the parameters set. This process is then repeated for each other class of vehicle as well as the number of chargers to ensure that every optimal solution along the entire Pareto Front is found. Using this method, the minimum number of class A vehicles to achieve no usage of gas is within the range of 26 and 31 vehicles.

The number of chargers has a significant effect on how the system operates.

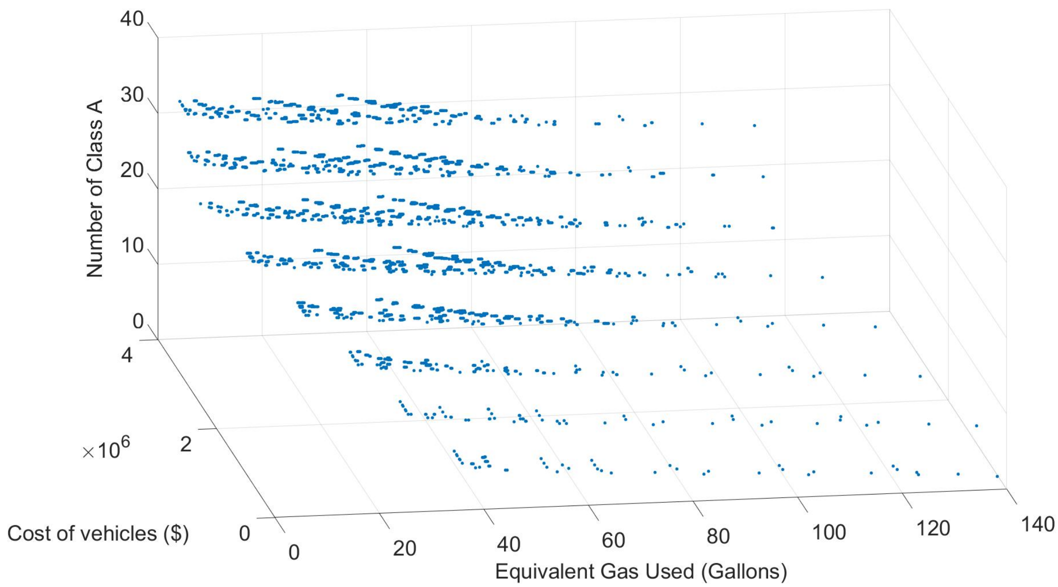

Figure 2.4: Total cost of vehicles versus gallons of gas used versus number of Class A vehicles for the parameters set in Table 2.2.

Figure 2.5 shows how the number of chargers affects the performance of the system. One can see that having the correct number of chargers is vital for the system to function as efficiently as possible. There are many cases where the system has an excessive number of vehicles but because there is a shortage of chargers, a system with fewer vehicles but more chargers is able to outperform it.

For example, looking up at the data above the point within the right most circle, there is a range of colors. These represent the cases where more vehicles may be purchased but because there are not enough chargers, the overall system does not function as efficiently. There is also a significant gradient of colors in the horizontal direction. Typically, systems that perform worse–with respect to amount of gas used–have less chargers in their system.

Figure 2.5 highlights two points which represent the optimal solutions. Test point one located on the y-axis shows the case that optimizes the system to use fully electric vehicles while reducing the cost as much as possible. This test point has multiple possible solutions to get the indicated result. Each one includes 31 class A vehicles, 7 class B vehicles, 31 class C vehicles, and 45 chargers. This result is expensive but due to the large amount of vehicles, it can always meet the job requirements. The second highlighted point shows test point two, which indicates where the slope of the Pareto front, shown in Figure 2.3, changes. This area represents the cases where the rate of reduction in fuel use begins to decrease with respect to the cost. These test points have a number of combinations of parameters that achieve the same result. Each case has 1 class A vehicles, 7 class B vehicles, 21 class C vehicles and a range of chargers from 30 to 45. This simulation point minimizes the number of expensive class A vehicles while reserving the chargers for the class B and C vehicles which are cheaper and faster charging in terms of SOC. With a cost of over three and a half times less than test point one, the system can reduce gas usage to around 33% of a system with only 1 vehicle in each class.

Two parameters that did not seem to influence the results of the simulation were the availability and SOC weights used to determine the charging order despite having a wide range. Figure 2.6 shows how neither variable affects the final solution in a quantifiable way. There is no pattern in the color scheme which represents the availability weights and no discernible change between each layer which is representing the SOC weights. It should be noted that the right side of the plot

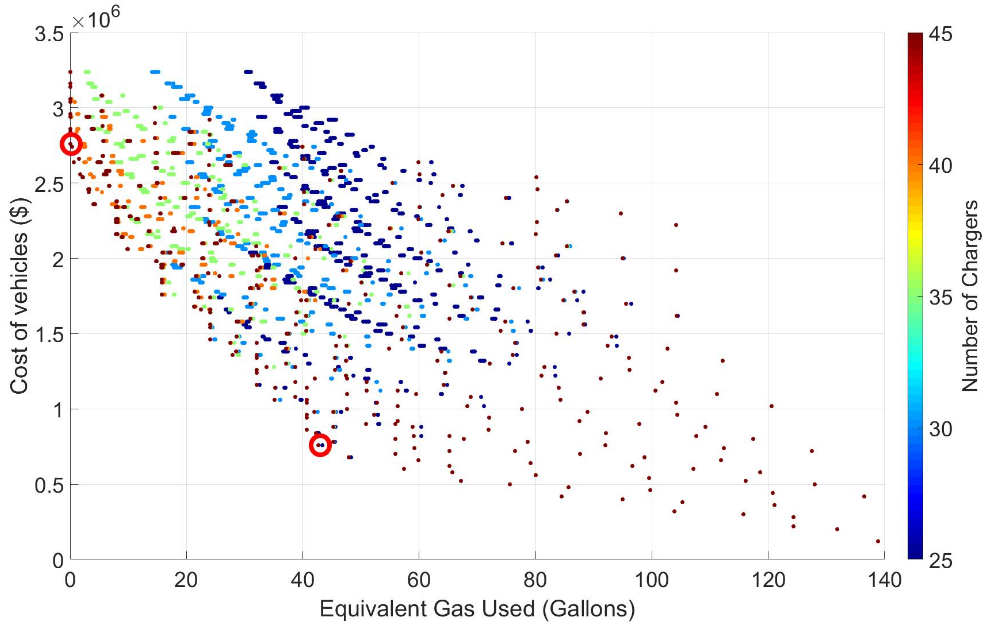

Figure 2.5: Total cost of vehicles versus gallons of gas used versus number of chargers for the parameters set in Table 2.2.

seems to show only blue dots but in reality, there are multiple data points under them. This means the results are the same despite the changing weights. One potential cause of this is due to both of these variables being a function of SOC. SOC is a function of only one vehicle while availability is calculated between all the vehicles within one class.

Overall, it is clear that using a charging algorithm improves the performance of the system. By implementing the same constraints on an identical system that does not use a charging algorithm but allows for random charging, a decrease in performance of 5-8% is found for test point two, while test point one uses a small amount of gasoline and no longer can fully operate on electric vehicles

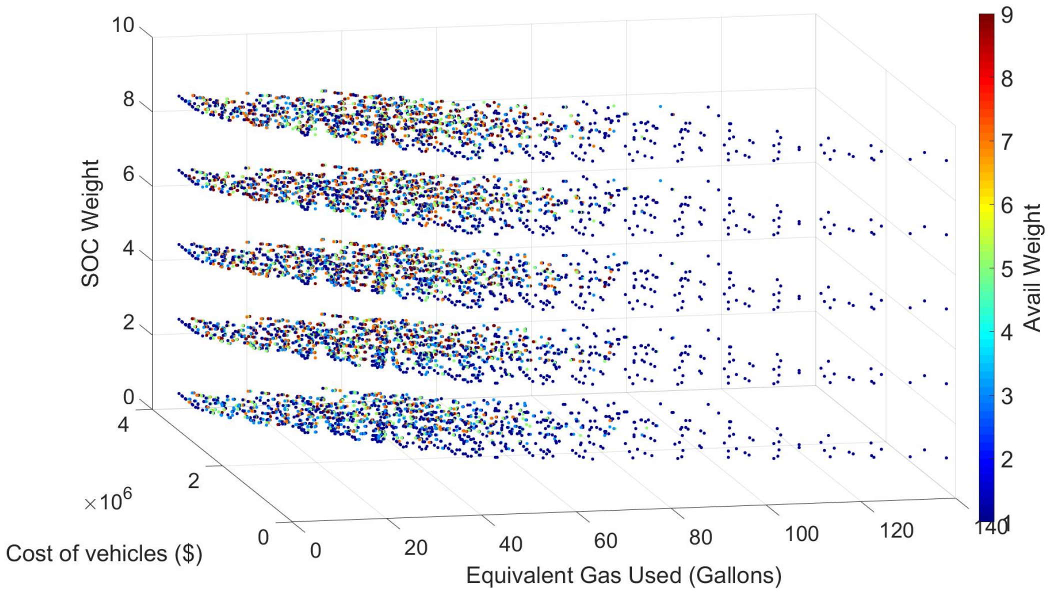

Figure 2.6: Total cost of vehicles versus gallons of gas used versus SOC weight and color coded by Availability weights

alone. This comparison with a "naïve" charging model shows how important it is to intelligently charge a fleet of vehicles within a system such as an electrified airport. Even the most basic of charging algorithms can increase performance and reduce the cost of both vehicles and electricity.

2.5 Conclusion

This paper models how a futuristic airport with electrified ground support vehicles can be constructed within the specific set of constraints given. It also illustrates how a Monte Carlo simulation can then be implemented and the concept of the

Pareto Front can be used to find multiple optimal points for the system with a given specific set of constraints. This method of optimization is recommended with similar systems of unknown behavior that contain a large number of tunable parameters.

Because of the tangential nature and limited number of works regarding electrified airports, there are a number of areas that could be delved further into as future work. The efficiency of the system including the vehicles, chargers, and overall distribution within the airport could be modeled with a higher level of detail. The cases tested are also quite coarse due to the large matrices that are created which cause significant delay in simulation run time. One way to get alleviate this issue would be to use a computer cluster or other high powered simulation hardware that can handle the large amount of data. Parallel computing is also an option to help speed up the simulation. The process of battery charging could also be explored which could change how the system operates in regards to how quickly vehicles reach full charge. Some factors such as the amount of energy used by a vehicle and daily energy consumption of the airport would need to be found experimentally over a period of time and then properly aggregated.

Chapter 3: Analysis of a Purpose Built Charger for Ground Support Vehicles in an Electrified Airport

3.1 Introduction

In regards to the current trends within the automotive industry, it is undeniable that one of the biggest pushes is the move towards electrification. Regulations are getting tighter and people are becoming more aware of the exceptionally low efficiency and large negative environmental impact of internal combustion engines [14, 15, 16]. To comply with the changing public demand and regulations, many companies have begun to look towards electrification while rapidly changing their business model to follow suit.

One such industry that also has its eyes on the future of electrification is the aviation industry. While it is generally accepted that all-electric aircraft are still many years out, the vehicles that service the airplanes are a prime target for electrification [1, 2, 3]. Maintaining this fleet of ground support vehicles does pose a number of challenges with the largest being the time it takes to charge an electric vehicle versus the time it takes to refuel a conventional gas or diesel vehicle. This makes quick, efficient and intelligent charging a necessity.

Another challenge is that the various vehicles required by an airport come in many shapes in size; both physically and electrically. Vehicles responsible for moving food, fuel, and waste are similar to large on road vehicles with battery voltages of up to 350 volts or potentially even more [17, 18]. Smaller vehicles that move luggage carts have battery voltages around 48 volts [19]. Having vehicles of various voltages require either on-board chargers which add cost or a single charger that needs to have a wide operating range and can handle many different power and voltage levels.

This paper focuses on the latter option of having an off-board vehicle charger that is capable of charging each vehicle regardless of its battery voltage. This reduces the number of chargers required by the airport thus lowering the cost of chargers required. Each vehicle will also not require a charger which would lower their cost. First, this paper will analyze traditional battery chargers along with the proposed. Next, it will move into analyzing the circuit at a component level using PLECS software. Finally, the results of the simulation will be shown and discussed.

3.2 Background

Traditionally, on-road vehicles carry most of the components of the battery charger within the vehicle. This allows for the vehicle to be able to adapt to whatever type of receptacle, e.g. 120 VAC, 240 VAC, that it has access to. There are also many off-road and industrial vehicles that carry on-board chargers. This is the easiest solution for typical use due to most applications only requiring a few vehicles and the easiest way to charge them would be to use a standard receptacle. The proposed application of the electrified vehicles within an electrical airport looks to break this tradition and remove the battery charger from the vehicle. This would allow for lighter, less complex vehicles as well as requiring a number of chargers potentially less than the total number of vehicles when deployed as a fleet.

Figure 3.1 shows a traditional on-board charger schematic [20]. This schematic is broken down into various sections including rectification, power factor correction, high frequency inverter, and high frequency rectifier.

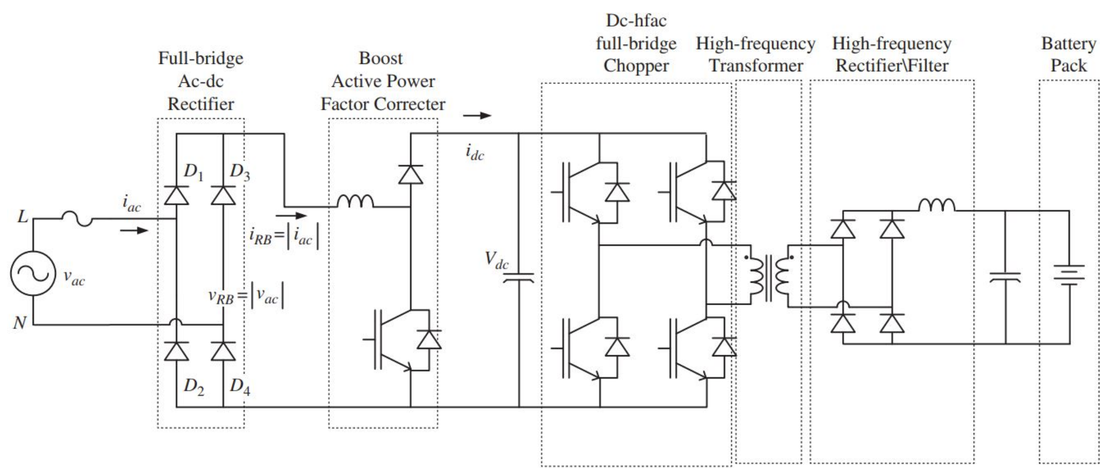

Figure 3.1: Typical on-board battery charger schematic [20]

First, the AC power enters the charger and goes through a full bridge diode rectifier. Within this section, complementary diodes conduct the AC power depending on which half wave cycle is being inputted. The output of this section is a fully rectified wave.

Next, it enters the power factor correction stage. The goal of the boost power factor correction (PFC) and DC link capacitor stage is to increase the power factor

(PF) as seen by the grid. For larger machines, having a high power factor makes the grid more efficient as well as saves the user money because a higher percentage of the total power used is real power. PF is made up of two parts: displacement and distortion. Displacement describes the phase shift between the voltage and current while the distortion describes the amount of unwanted harmonics in a signal. This relationship is shown in Equation 3.1 where PF is ideally 1.

$$PF = \text{Displacement} \cdot \text{Distortion} \tag{3.1}$$

In regards to how PF is calculated moving forward in this paper, it is assumed that the PFC stage is putting the voltage and current waveforms in phase with each other. This means that the PF of the AC power is only based on the distortion factor. This distortion is calculated based on the total harmonic distortion (THD) contained within the signal. THD is the sum of magnitudes of harmonics within a signal with respect to its fundamental frequency. This is shown as

$$THD = \frac{\sqrt{\sum_{n=2}^{\infty} X_n^2}}{X_1} \tag{3.2}$$

where X_1 is the magnitude of the fundamental frequency and X_n is the magnitude of the *nth* frequency. Ideally, this value is 0. To use THD to calculate PF, Equation 3.3 is used.

$$PF = \frac{1}{\sqrt{1 + \text{THD}^2}} \tag{3.3}$$

The PFC section of the charger operates similar to a traditional boost converter in the sense that it charges and discharges an inductor in series with the source to increase the voltage. To accomplish this, the IGBT is modulated so that the current through the inductor is sinusoidal and in phase with the input voltage coming in from the source. This inductor current is shown in Figure 3.2. PFC is done to reduce distortion of the input current and increase the power factor as seen by the grid. Figure 3.3 shows the input current of a system with and without a boost PFC stage. The example system equipped without PFC has a THD of 0.813 (PF of 0.776) and the one with PFC has a THD of 0.231 (PF of 0.974).

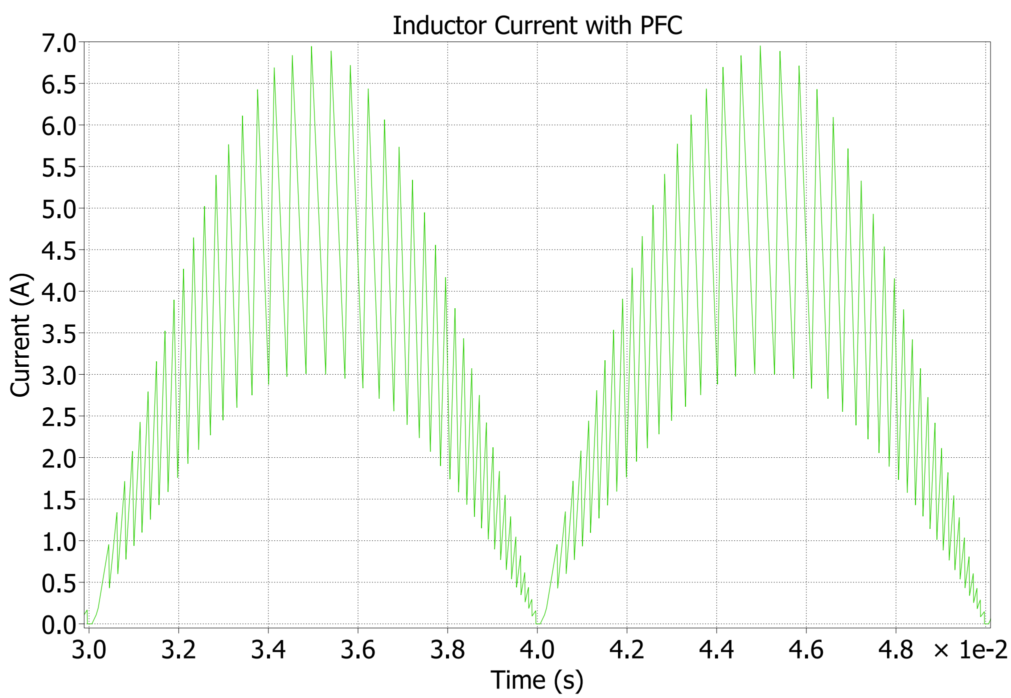

Figure 3.2: Inductor current in a sample system using boost PFC

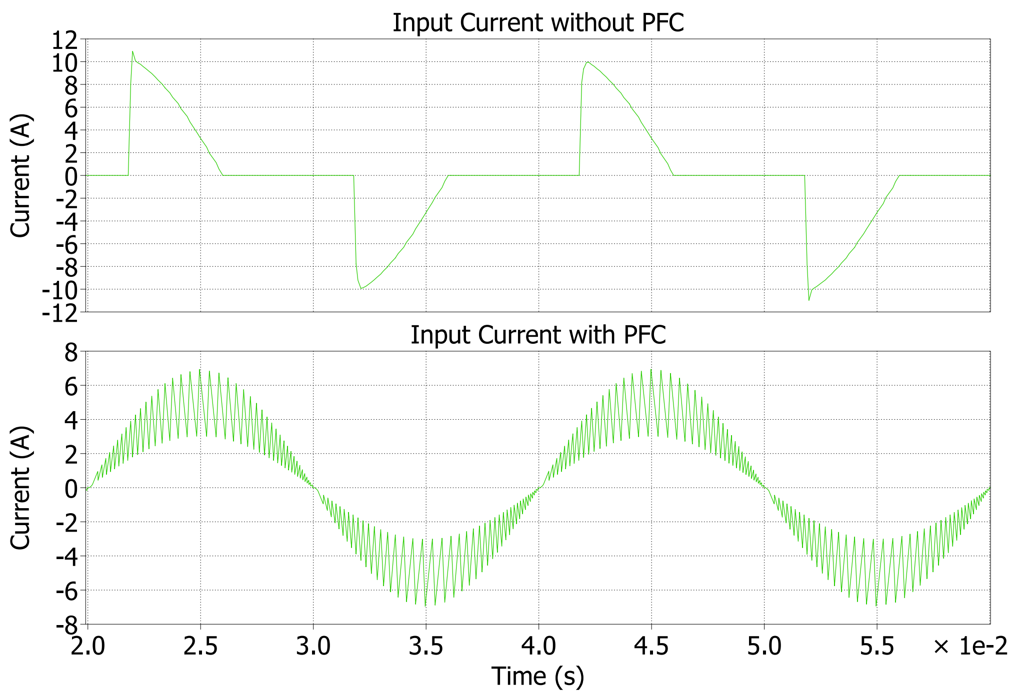

Figure 3.3: Input current of a sample system without and with boost PFC

The controls of the PFC system come down to the how the IGBT is switched. To calculate the ever changing duty cycle, the input voltage, inductor current, and voltage set must be inputted into a cascaded control loop. The outer voltage loop determines the amount of current required to meet the output voltage set point with the current load. The inner current loop then regulates the current through the inductor such that the average current through the inductor both follows the input voltage as well as maintaining the proper output voltage set point.

The output voltage of the boost PFC section is then used to charge a large DC link capacitor. Ideally, this capacitor is large enough so that the voltage across it is always constant.

The next stage of the traditional battery charger is the high frequency (HF) inverter circuit. This stage has two main functions. The first is to create a HF AC waveform to pass through the transformer and the second is to set the output voltage.

The physical layout of the inverter section includes two power poles. A power pole is defined as two IGBTs and their body diodes connected in series. The top and bottom of the two poles are connected to each side of the DC link capacitor. The middle of each power pole is then connected to the input of the transformer.

Despite there being two common methods of switching, they both have many similar characteristics. For example, both switching types use comparator logic between a triangular (carrier) wave and a reference wave to operate. The carrier waveform is set at the switching frequency which is much greater than the frequency of the reference waveform. The reference wave is created in the shape and frequency of the desired output. In the case of a DC-AC inverter, it is a sine wave. The switches modulate on or off depending when the carrier is either greater or less than the reference.

Both types of switching also function the same to control the output peak value by way of the modulation index (M_a). M_a is defined as the ratio of the desired amplitude of the output to the input which is the same as the ratio between the reference and carrier amplitudes. Equation (3.4) shows how M_a is calculated.

$$M_a = \frac{V_{out,peak}}{V_{DC}} = \frac{A_{ref}}{A_{cr}} \tag{3.4}$$

One type of switching is bipolar switching which operates all 4 switches as two complementary pairs at the same time [21]. Complementary pairs are defined as two switches that are on opposite power poles and diagonally placed according to the schematic shown in Figure 3.1. This results in an output voltage that is either positive or negative at all times. Figure 3.4 shows that how the reference waveform moves through the carrier waveform. The comparison is done between the two to get the duty cycles of each power pole and the total voltage output is shown at the bottom.

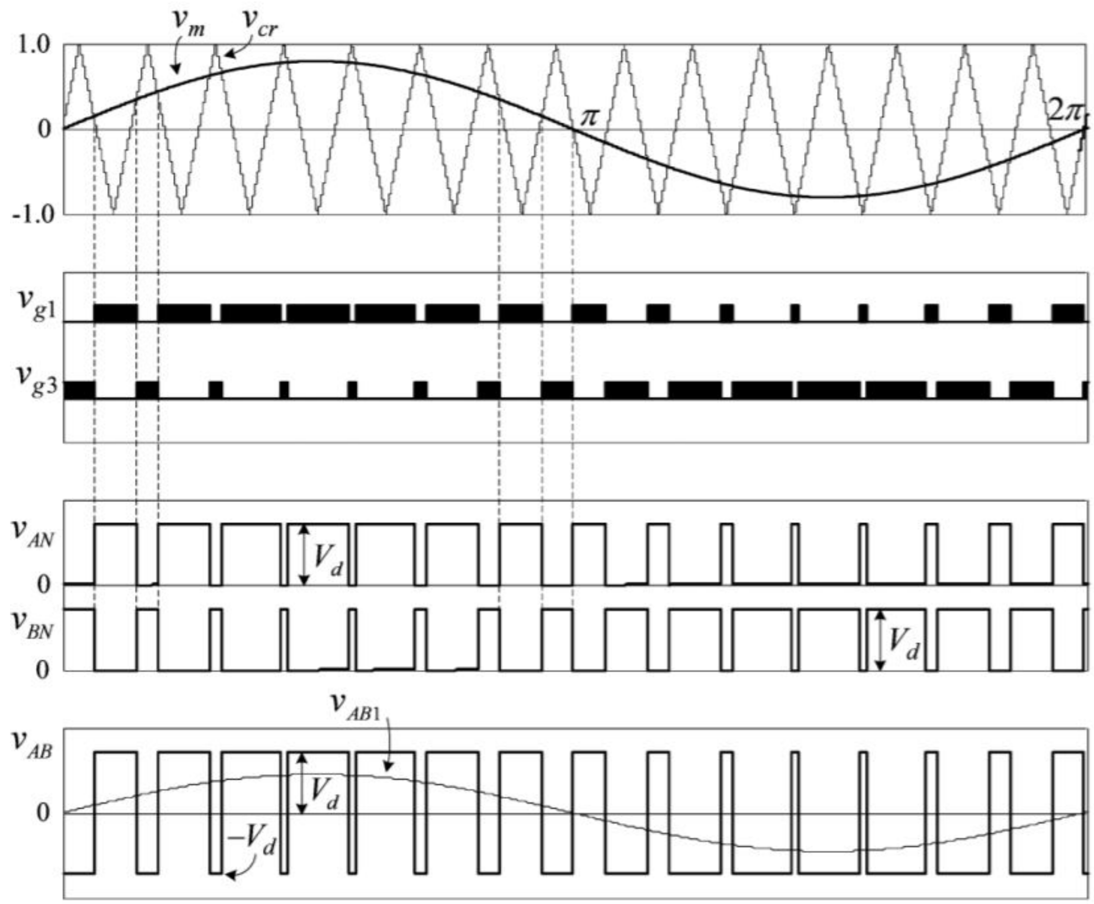

Figure 3.4: Comparator, switching, and output waveforms for an inverter using bipolar switching techniques [21]

Unipolar switching operates in a similar method except there are two reference waveforms being compared; one for each power pole. These two reference waveforms pass through the carrier waveform while being phase shifted by 180 degrees. Because of this, the power poles operate independently while switches on the same power pole operate complementary. This allows for 3 potential outputs; V_{dc}, 0, and

$-V_{dc}$. Figure 3.5 shows how the comparison between the carrier and two reference waveforms work with each power pole set of switches. It also shows the range of output voltages that are able to be realized.

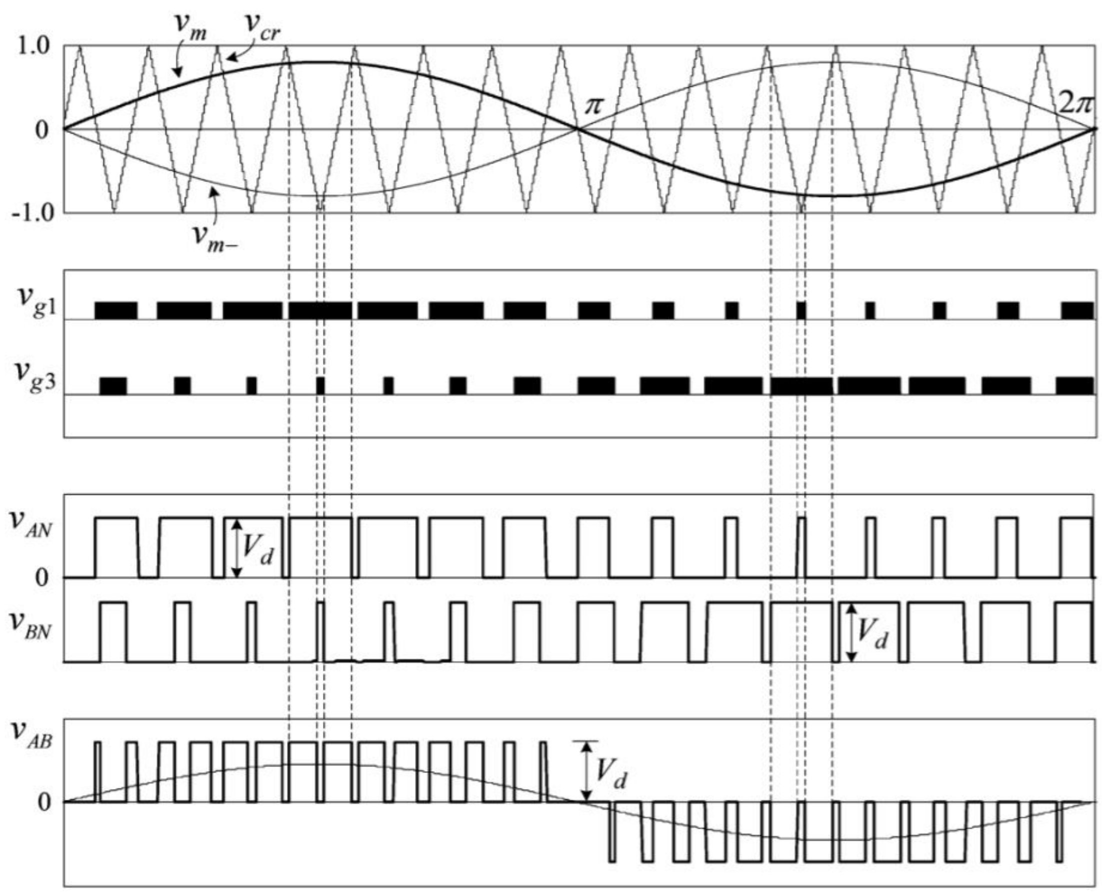

Figure 3.5: Comparator, switching, and output waveforms for an inverter using unipolar switching techniques [21]

Regardless of the method of switching that is used, DC voltage is converted into a HF AC voltage that is passed on to the transformer stage. The high frequency allows for the physical size of the transformer to be decreased which makes for easier on-board packaging and weight reduction of the vehicle. The transformer also works as galvanic isolation [22].

After passing through the HF inverter, the peak voltage of the HF AC waveform is already set to the required DC voltage by way of the M_A. After the transformer, the high frequency AC is rectified back into DC using a full bridge rectifier. It is then filtered before being sent to the battery pack as a DC signal.

3.3 Proposed Charger

One of the biggest drawbacks regarding the components within the charger shown in Figure 3.1 is the number of unidirectional switches or diodes. There is potential to increase the efficiency as well as add features such as vehicle-to-grid (V2G) by reducing and modifying the type of switches used. While V2G is mostly conceptual right now, it is a technique that could be viable in the future [24]. This proposed battery charger focuses on reducing the number of switches to redesign the battery charger circuit.

3.3.1 Charging

Figure 3.6 shows this conceptual charger. This charger is broken down into 4 sections. Compared to the traditional charger, the most visually different section is the multi-tap transformer near the AC source. This transformer would take in AC voltage and be able to deliver different AC voltages into the system. This allows for the rest of the system to function at similar operating points while delivering different output voltages. One aspect of this transformer that would differ from the one in the traditional charger would be that this transformer would be operated at a lower frequency. This requires the transformer to be physically larger. For an on-board charger, this would be problematic but for the proposed off-board charger, size and weight are less of a constraint.

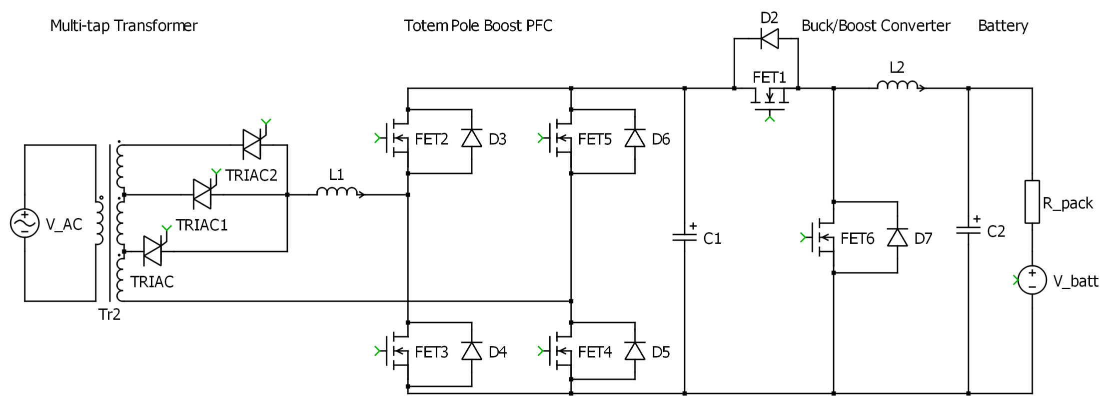

Figure 3.6: Proposed battery charger divided into sections

Next, the AC waveform enters the totem pole PFC stage. This section replaces the five diodes, one IGBT, and an inductor with 4 SiC MOSFETs and an inductor. The totem pole PFC functionally operates the same as the traditional boost PFC. It takes in an AC waveform and modulates the current through the inductor to be in phase with the input voltage thus increasing the power factor.

The right-most pole is the slow switching pole. The switches are turned on and off in complementary fashion according to which half cycle of the AC waveform is currently flowing through the input. The left most power pole is the fast switching pole. The non-boost MOSFET switches according to Equation 3.5 during each half wave cycle of the AC waveform [20]. The non-boost MOSFET is the top switch during the positive half cycle and bottom during the negative.

$$D = 1 - \left| \frac{\sqrt{2} \cdot V_{\text{rms}} \cdot \cos\theta}{V_{DC}} \right| \tag{3.5}$$

As previously mentioned, both high and low speed switches are dependent on the AC waveform. When it is positive, the bottom slow switch is always on and the top fast switch is modulated according to the duty cycle from Equation 3.5. The bottom fast switch switches complementary to the top. Figure 3.7 shows the current flow through both switches during a positive waveform. When the negative half cycle is input to the system, it functionally performs opposite or as shown in Figure 3.8.

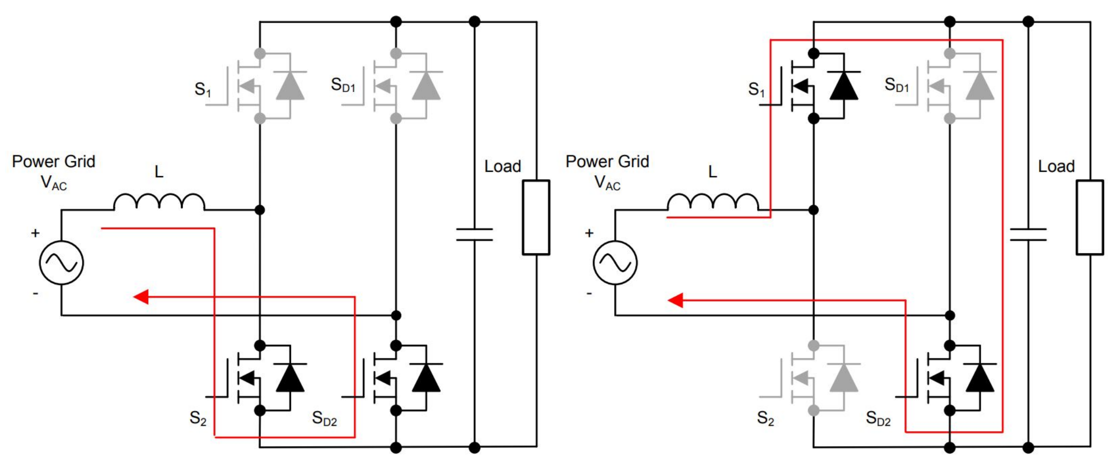

Figure 3.7: PFC stage operation during the positive half cycle of the AC waveform [26]

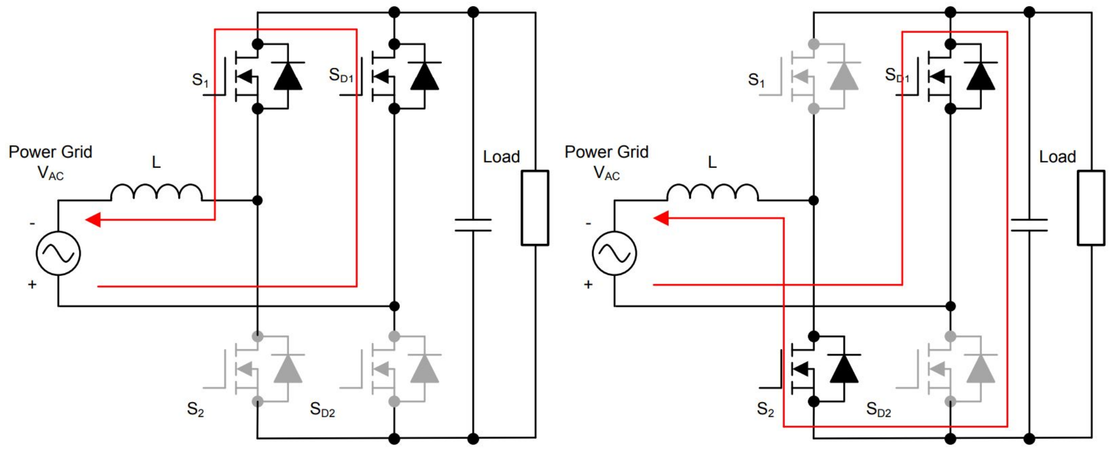

Figure 3.8: PFC stage operation during the negative half cycle of the AC waveform [26]

This duty cycle is controlled similar to the traditional boost PFC in the sense that it is controlled by two cascaded controllers shown in Figure 3.9. The outer voltage loop sets the output DC voltage and the inner current loop sets the instantaneous current through the inductor to follow the input voltage waveform. The voltage loop uses a traditional proportional-integral (PI) controller while the current loop uses a proportional-resonant (PR) controller.

A PR controller is used to control the current because of the rapidly and always changing set point. A traditional PI controller would need an exceptionally high integral gain to function properly and eliminate the steady state error. This can make the controller unstable at times [27]. A PR controller has an excessively high gain at a specific frequency which can be set at the input frequency of the voltage to help reduce and nearly eliminate steady state error. To accomplish this same task in a system using DQ control, the method presented in [28] or a three phase

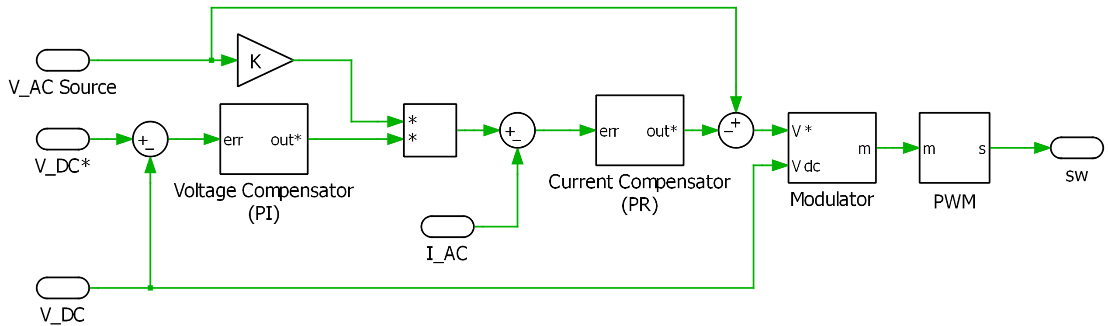

Figure 3.9: Totem pole PFC cascaded controllers

input would be used.

The DC output of the totem pole PFC goes into a large DC link capacitor to smooth the voltage. The DC voltage is then fed into a traditional buck converter. Here the boosted DC voltage is lowered to the voltage the battery requires to charge. The upper MOSFET switches according to the required duty cycle D as calculated in Equation (3.6). When the upper MOSFET is off, the body diode of the lower MOSFET conducts to allow the inductor and capacitor to discharge thus smoothing out this chopped waveform. By using the multi-tap transformer, this buck converter section should be able to run at a similar operating point despite charging different vehicles while at the same time remaining within a reasonable operating limit [29].

$$D = \frac{V_{\text{out}}}{V_{\text{in}}} \tag{3.6}$$

The battery model contains two sections: the components within the charging circuit and the SOC circuit outside the charging circuit. The physical battery is modeled as a simple resistor and a voltage controlled voltage source as seen in Figure 3.10. The simple model is usable due to the low number of significant dynamic changes that would occur during charging. If desired, a complete dynamic model can be found in [30, 31, 32]. The series resistor models the internal resistance of the battery pack and is typically experimentally calculated. Its value is a function of SOC but is approximately constant within normal operating conditions as shown in [30]. It can be estimated by finding the resistance of one cell and then knowing the number and configuration of cells within the pack. In other words, the internal resistance can be calculated by

$$R_{\text{pack}} = R_{\text{cell}} \cdot \frac{N_s}{N_p} \tag{3.7}$$

where R_{cell} is the resistance of one cell, R_{pack} is the resistance of the whole pack, N_s is the number of cells in series, and N_p is the number of cells in parallel. The only drawback to this method is that it neglects the resistance over the other components within the battery such as cabling, fuses, and connectors. The value of the voltage controlled voltage source is dictated by the auxiliary circuit proposed in [30] that helps to set the state of charge (SOC) of the battery. As current flows in or out of the battery in the charger circuit, a current controlled current source sources or sinks charge from the ideal capacitor. The range of voltage over the capacitor moves between zero and one which corresponds to the battery's SOC ranging from zero to one hundred percent. The voltage of the capacitor is then correlated to an output voltage that is sent to the voltage controlled voltage source within the charge circuit. The capacitor value is defined as

$$C = 3600 \cdot \text{Capacity} \cdot f_{\text{cycle}} \cdot f_{\text{temp}} \cdot 2.778 \times 10^{-7} \tag{3.8}$$

where C is the capacitance in $\frac{kWhr}{V^2}$, Capacity is the capacity of the battery to be modeled in A-hr, 3600 converts from A-hr to coulombs of charge, 2.778×10^{-7} concerts from F to $\frac{kWhr}{V^2}$ and f_{cycle} and f_{temp} are cycle and temperature factors that could influence battery performance depending on past usage or environment. For this experiment, the temperature and cycle factors are ignored but more information on these factors can be found in [23].

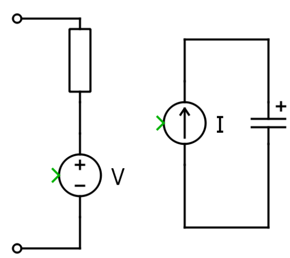

Figure 3.10: Battery model used to simulate a vehicle battery

3.3.2 Vehicle-to-Grid

The proposed charger also has the bidirectional ability to send power from the battery back to the grid in a method commonly called Vehicle-to-Grid or V2G. By enabling V2G, each section changes its control scheme to instead discharge the battery and send power back to the grid. This method would allow for the large amount of energy stored in the vehicles' batteries to be transferred back to the local grid to help with dynamic disturbances [24, 25].

In order to analyze the V2G mode, each section of the proposed charger will be examined starting at the power source or battery. Here DC voltage is sent into the DC/DC converter which now operates as a boost converter. As opposed to the buck converter, the lower MOSFET is now being modulated and the upper MOSFET is turned off. The boost converter works to boost the voltage by applying the input voltage over the inductor for the on stage of the duty cycle. During the off cycle, the inductor acts as a voltage source and is placed in series with the input source to increase the voltage. Equation 3.10 shows the relationship of the duty cycle D and the input and output voltages of the boost converter.

$$V_{out} = \frac{V_{in}}{1 - D} \tag{3.9}$$

The boosted DC voltage charges the DC link capacitor and is fed into what was the totem pole PFC stage while charging. While in V2G mode, this full bridge inverter operates using either bipolar or unipolar switching schemes described in Figures 3.4 and 3.5. The current set point is controlled using a PR controller which, as previously mentioned, allows for large gains at a fundamental frequency. In this case, the fundamental frequency is the grid frequency. This controller not only controls the amount of current to the grid, but also keeps the output current and grid voltage in phase to ensure a near unity power factor. The output voltage of the inverter is sent to the multi-tap transformer. Because the battery voltage is what the system reads to select which tap to use, the voltage that the inverter sends is dependent on the input voltage of the battery and its peak value is calculated by using the M_a. The voltage is scaled up to the correct input voltage of the grid through the transformer and transmitted.

3.3.3 Components

This section will examine specific design parameters that are required to operate the charger. This will include specific component values as well control values chosen to ensure the system is robust and reliable. This section will then go on to examine the results of various simulations within PLECS while in both charging and V2G modes.

The specific operating goals of the charger are shown in Table 3.1. With these goals in mind, specific components will be found to meet these theoretical specifications and tests will be run to ensure stable operation of the charger while running at various input and output conditions.

To meet these output goals, a number of parameters for the system are chosen by the designer. First, the grid voltage of 240 V RMS at 60 Hz is chosen to decrease the input current required. Having lower current equates to higher efficiencies and typically leads to smaller physical components and wire sizes. The switching frequency is also set at 80 kHz. This value was chosen to minimize switching losses in the MOSFETs and diodes as well as minimizing voltage and current ripples. The switching frequency was also chosen well out of the range of audible levels to

Table 3.1: Design goals of the off-board battery charger

Parameter	Value	Units
Input Voltage	240	VAC_{rms}
Input Current	33	A_{rms}
Switching Frequency	80	kHz
PFC Current Ripple	<5	% p-p
PFC Voltage Ripple	<10	% p-p
PFC Output Voltage	650	VDC
Buck or Boost Current Ripple	<10	% p-p
Buck or Boost Voltage Ripple	<5	% p-p
Max Output Power	8	kW

humans. The max output power was chosen as 8 kW as this product designed here would be competing with similar chargers at the same power level already being used for on-road vehicles.

Before specific components can be calculated for, it must be known what physical constraints they need to work within. One such component is the battery. With the use of the multi-tap transformer, the goal of the charger is to be able to charge all types of batteries. For this specific case, battery voltages of 48 V (small tug tractors), 96 V (large tug tractors), and 350 V (modified on-road vehicles) will be able to charge with this specific charger. Table 3.2 defines various attributes about each battery. The values are calculated assuming per cell voltages of 3.6 V nominal, 4.1 fully charged and 3.2 V fully discharged while internal resistance per cell is 70 mΩ [33]. The internal resistance is calculated by

$$R_{\text{batt}} = \frac{N_S \cdot N_{\text{packs}}}{N_P} \cdot R_{\text{cell}} \tag{3.10}$$

where N_S is defined as the number of cells in series, N_P is the number of cells in parallel, N_{packs} is the number of packs, and R_{cell} is the resistance of a single cell. The configuration of the battery describes how the cells are organized and number of packs is how many of them are in series with each other. For example, the configuration XpYs has Y cells in series and X cells in parallel in one pack. Parks are then arranged in series to increase the voltage. Having more packs allows for easier maintenance if one battery pack fails as well as having more redundancy if one cell fails.

Table 3.2: Specifications of various batteries to be charged using the proposed charger

Battery Voltage (V)	48	96	350
Discharged Voltage (V)	41	84	310
Charged Voltage (V)	53	106	390
Capacity (kW-hr)	50	102	100
Pack Configuration	316p13s	322p13s	86p6s
Number of Packs	1	2	16
Number of Cells	4108	8372	8256
Internal Resistance (mΩ)	3	5	78

When examining the internal resistance of the battery, it must be noted that these resistances are only the internal cell resistances. They do not include any resistance due to wiring, cabling, connectors, or fuses. When the model is run in PLECS with a very low internal resistance value, the simulation see it is as too close to zero and faults out. For both of these reasons, the 78 mΩ value will be used for each of the three battery types.

The most important component value that affects the largest function of the system is the totem pole boost inductor. In Figure 3.6 it is labeled as L1. Despite the topology being different than the traditional boost PFC, the method of calculating the inductor value remains the same [20]. The value of the inductor needs to be large enough to ensure minimal ripple while at the same time, minimizing distortion of the input waveform.

The ripple inductor is calculated by Equation 3.11. The speed of switching (f), input phase voltage (V_{ph}), and the desired ripple current (ΔI_{rip}) all are factors in finding the value of the inductor (L). The condition that requires the largest inductance is when a 350 V battery is being charged.

$$L = \frac{\sqrt{2} \cdot V_{ph} \cdot D}{f \cdot \Delta I} = \frac{\sqrt{2} \cdot 240 \cdot 0.478}{80000 \cdot 2.33} = 869\ \mu H \tag{3.11}$$

where ΔI_{rip} is calculated as

$$\Delta I_{rip} = 0.05 \cdot 33 \cdot \sqrt{2} = 2.33\ A \tag{3.12}$$

and according to [20] the maximum value of D is found by

$$D = 1 - \frac{\sqrt{2} \cdot V_{ph}}{V_{dc}} = 1 - \frac{\sqrt{2} \cdot 240}{650} = 0.478. \tag{3.13}$$

The DC link capacitor has a large role in how the voltage is conditioned before being sent to the buck or boost sections. In the same way that a boost converter can not operate without a capacitor filter on the output, the totem pole boost PFC circuit is no different. Not only that, the output voltage needs to remain stable so the voltage control loop in the PFC controller can operate properly. The

DC link capacitor's job is to filter out the low frequency created by the rectifier. This frequency is two times the input frequency. The worst case scenario for this capacitance is when a 48 volt vehicle is being charged. The value of the capacitor is calculated by

$$C = \frac{I_{out,peak} \cdot D}{\Delta V_{rip} \cdot f} = \frac{20 \cdot 0.478}{10 \cdot 2 \cdot 60} = 7.97\ mF \tag{3.14}$$

where D is the calculated duty cycle from 3.13 and ΔV_{rip} is

$$\Delta V_{rip} = 0.1 \cdot 100 = 10\ V. \tag{3.15}$$

The value of the inductor and capacitor in the buck or boost converter can also be determined based on a desired output current and voltage ripple. By rearranging the fundamental inductor equation, Equation 3.17 is found where L is inductance, V_L is the voltage over the inductor, f is the switching frequency and D is the largest duty cycle which would occur while the converter is operating in buck mode. The worst case scenario that would require the largest inductance is when a 350 V vehicle is charging. D is calculated by

$$D = \frac{V_o}{V_{in}} = \frac{390\ V}{650\ V} = 0.6. \tag{3.16}$$

$$L = \frac{V_L \cdot D}{f \cdot \Delta i} = \frac{(650 - 310) \cdot 0.6}{80000 \cdot (0.1 \cdot 20)} = 1.28\ mH \tag{3.17}$$

Because the value of the inductor was designed to operate in continuous conduction mode (CCM), it is important to note when it would enter discountinuous current mode (DCM). DCM typically occures during light load conditions and is defined as when the inductor current goes to zero for part of the cycle. In other words when

$$I_{rip} > I_{out}. \tag{3.18}$$

To calculate the current load at which this would occur, Equation 3.19 is used. By finding the equivalent critical resistance and knowing the max output voltage Ohm's Law can be used and a minimal charging current can be found.

$$I_{min} = \frac{V_{out} \cdot D}{2 \cdot L \cdot f_{sw}} = \frac{390 \cdot 0.6}{2 \cdot 0.00128 \cdot 80000} = 1.14\ A \tag{3.19}$$

The capacitor value of the buck or boost converter controls the amount of voltage ripple that is seen by the output. By knowing the desired ripple as well as the switching frequency, output current, and duty cycle, a capacitor value can be found. The worst case scenario for this capacitor occurs when a 48 V vehicle is charged.

$$C = \frac{I_C \cdot D}{f \cdot \Delta V} = \frac{20 \cdot 0.53}{80000 \cdot 0.05 \cdot 41} = 65\ \mu F \tag{3.20}$$

where D is calculated as

$$D = \frac{V_o}{V_{\text{in}}} = \frac{53}{100} = 0.53. \tag{3.21}$$

An important factor to consider when designing a system such as a battery charger is the efficiency. Having an efficiency of 100% would be ideal but this is rarely feasible due to parasitic resistances within the circuit. While each component, wire, trace, and connector will have a small power loss associated with it, the area that loses the most power is within the switching semiconductors. For this reason, the choice of semiconductors chosen plays a large factor in this overall efficiency.

An ideal MOSFET would be represented as an ideal switch where it is either on or off but a realistic MOSFET has two types of losses: conduction and switching. Conduction losses are simpler to understand and they can be modeled by having a small resistance ($R_{\mathrm{DS,on}}$) in series with an ideal switch. This is due to the semiconductor having a small forward voltage drop (V_f) over it and as current passes through the MOSFET (I_D), power is lost. This relationship is shown in Equation 3.22.

$$P_{\mathrm{cond}} = R_{\mathrm{DS,on}} \cdot I_D^2 \cdot D \tag{3.22}$$

Switching losses are more complicated. Before the switch is triggered by an external control circuit at its gate to turn on, the drain-source voltage (V_{DS}) is high and current is 0. Once the external control circuit decides to turn on the MOSFET, voltage is applied to the gate (V_{GS}). Because the MOSFET is a voltage controlled and capacitive device, the voltage rises slowly. The voltage will rise to a point called the threshold gate voltage ($V_{\mathrm{GS,th}}$). Once this point is reached, current through the device (I_D) begins to flow and ramps up towards its set current. At this same time, V_{GS} is still at the initial value. As V_{GS} continues to increase, it will eventually reach the Miller Plateau. Here, I_D reaches its max value and V_{GS} begins to decrease. Once the V_{DS} reaches its forward drop voltage (V_f), V_{GS} will continue to rise to the set value by the external control circuit. When the MOSFET turns off, the cycle is reversed. This turn on cycle is shown in Figure 3.11.

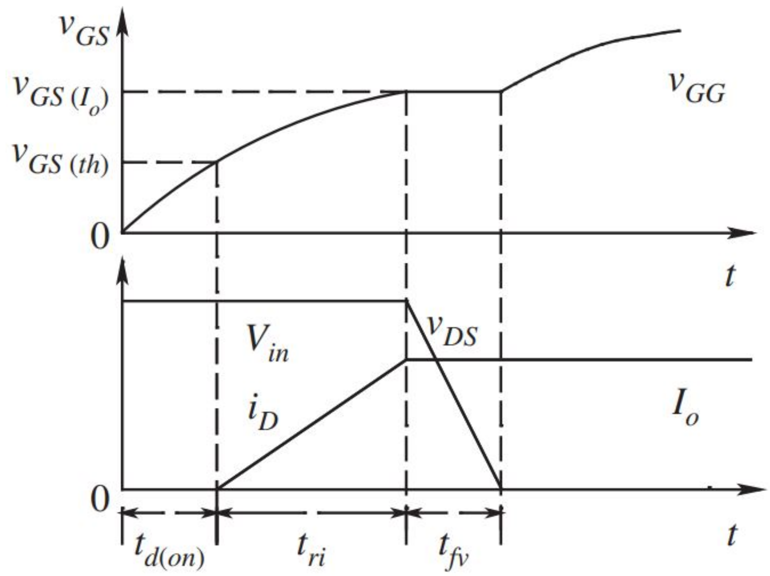

Figure 3.11: MOSFET turn on waveforms [34]

Power is lost during each switching cycle when current is flowing through the device while there is a voltage drop. Equation (3.23) describes this loss.

$$P_{\text{sw}} = (E_{\text{on}} + E_{\text{off}}) \cdot f_{\text{sw}} \tag{3.23}$$

where E_{on} is defined as

$$E_{\text{on}} = \frac{1}{2} \cdot V_{\text{in}} \cdot I_D \cdot (t_{\text{ri}} + t_{\text{fv}}) \tag{3.24}$$

and $t_{\text{ri}} + t_{\text{fv}}$ is defined in Figure 3.11. E_{off} is calculated using the same equation and $t_{\text{ri}} + t_{\text{fv}}$ becomes $t_{\text{fi}} + t_{\text{rv}}$.

The MOSFETs that are chosen for the system play an important role in finding the overall system efficiency. For this high voltage, high current application, silicon carbide (SiC) MOSFETs were chosen. Some advantages of SiC MOSFETs include lower $R_{\text{DS,on}}$ values,high blocking voltages, and fast turn on/off times to reduce switching loss. One disadvange to SiC MOSFETs is that the intrinsic diode that is within the MOSFET package typically has a large forward voltage drop which is typically offset by the use of a fast recovery or Schottky diode [35]. The chosen MOSFETs for this battery charger are BSM120D12P2C005 for the PFC MOSFETs while C3M0030090K is used for the switches within the buck or boost section. Individual attributes of each MOSFET is shown in Table 3.3 [36, 37].

Table 3.3: Attributes of chosen MOSFETs

Part Number	Voltage (V)	Current (A)	$R_{\text{DS,on}}$ (mΩ)
BSM120D12P2C005	1200	134	30
C3M0030090K	900	63	30

These chosen MOSFETs have high voltage ratings so as to not be affected by the large DC voltages within the charger. They also have high current ratings to be able to handle steady state use as well as large inrush current that will occur at start up. Another aspect to note about the chosen MOSFETs is that these specific MOSFETs were partly chosen because of the availability of their thermal data and ease of implementation into the PLECS software. This thermal data allows for more precise calculations of the switching and conduction loses as compared to using static values. Overall, they make for a more realistic model if these MOSFETs were implemented.

One key difference between the duty cycle calculation shown in Equation 3.5 and how PLECS uses a duty cycle is that a traditional duty cycle runs between zero and one while PLECS uses a value between negative one and one. This results in a different duty cycle equation. Equation 3.25 shows how this duty cycle in PLECS is calculated. This duty cycle is calculated for the non-boost MOSFET of each half cycle waveform. The equation is still derived from the same duty cycle equation of a boost converter while being scaled up to the new range required by PLECS. It also creates the complimentary pattern shown in Figure 3.12 to accommodate both of the MOSFETs in the totem pole configuration.

$$D = \frac{\sqrt{2} \cdot V_{\mathrm{rms}} \cdot 2 \cdot \cos\theta}{V_{DC}} \pm 1 \tag{3.25}$$

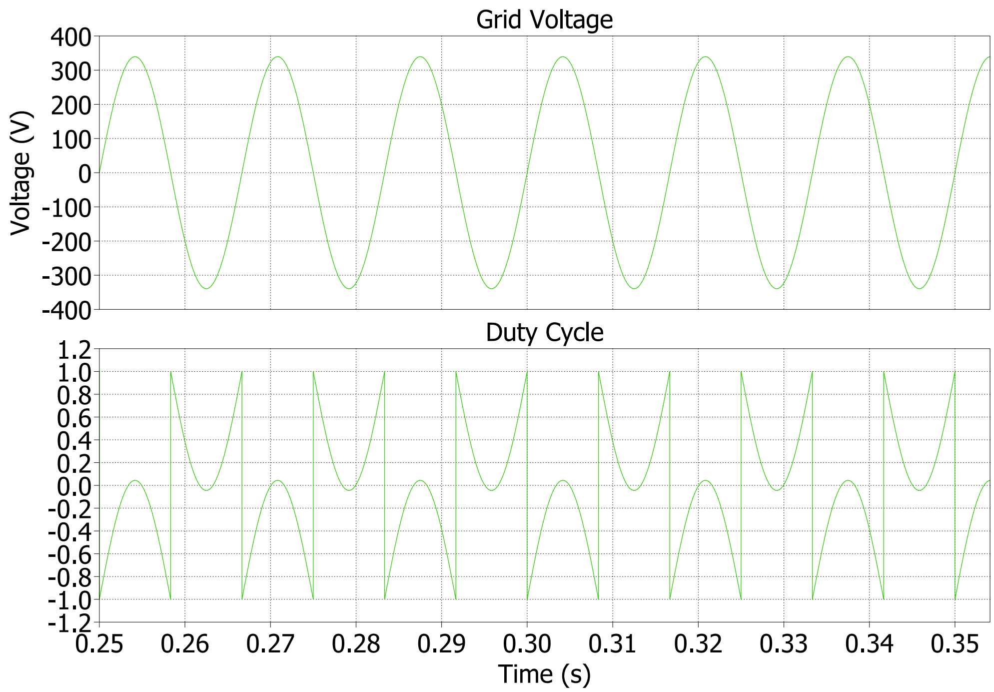

Figure 3.12: Duty cycle of the non boost MOSFET as calculated within PLECS

Within the efficiency calculation for this specific charger, the only components that are included is the MOSFETs and their diodes. This is due to the minimal losses within other components compared to the MOSFETs as well as the inability to limit or design out parasitic losses such as wire, trace and capacitor (ESR) resistances.

It must also be noted that PLECS is not the ideal design tool for a total thermal system. This is due to the fact that PLECS is designed to run only for short periods of time. For a system as large and as complex as this proposed battery charger, run times become difficult if not impossible for the experimental values to reach steady state in a reasonable amount of time. To account for this, the thermal capacitance of the system will be reduced to help the system converge to a steady state temperature as fast as possible.

Table 3.4 shows the experimentally determined power losses. These losses were found using the PLECS simulation. This was due to the PLECS software not taking into account the V_{GS} value while finding the losses.

Table 3.4: Power losses of switching components

MOSFET/Diode	High Speed PFC	Low Speed PFC	Buck or Boost
R_{js} (°C/W)	0.235	0.235	0.735
Conduction (W)	10	9	16.1
Switching (W)	112	0	45.5
Amount	1	2	2
Total Loss (W)	244	18	123.2
Total (W)			323.6

The thermal management system will attempt to keep the sink temperature around 65°C. With the given R_{js} value of the MOSFETs and the total power lost, this sink temperature should keep the buck or boost section MOSFET around 110°C. One important note is that this value was found while the devices were ambient temperatures and so as the device temperature increases, so will the losses. Because of this, a slightly larger heat sink than calculated will be needed.

To calculate temperatures at specific points, a thermal model is used. This model uses Ohm's law where current becomes power, resistance becomes thermal resistance and voltage becomes temperature. A modified Ohm's Law is then used as shown in Equation 3.27.

$$T = P \cdot R \tag{3.26}$$

By knowing the total power lost, the R_{js} values of each MOSFET, and the target temperatures of the heat sink and MOSFET junction, a thermal resistance of a heat sink can be found.

$$65 - 25 = 324 \cdot R \tag{3.27}$$

where R is found to be 0.123 while will be rounded up to 0.1 °C/W to account for increased losses at higher temperatures. This results in a junction temperature of the buck or boost MOSFET of around 110 °C. Figure 3.13 shows how this value plateaus near this value. As previously mentioned, the values were calculated when their temperatures were near ambient. As they increase, more losses will be incurred. Thus, a slightly larger heat sink must be designed to accompany this design.

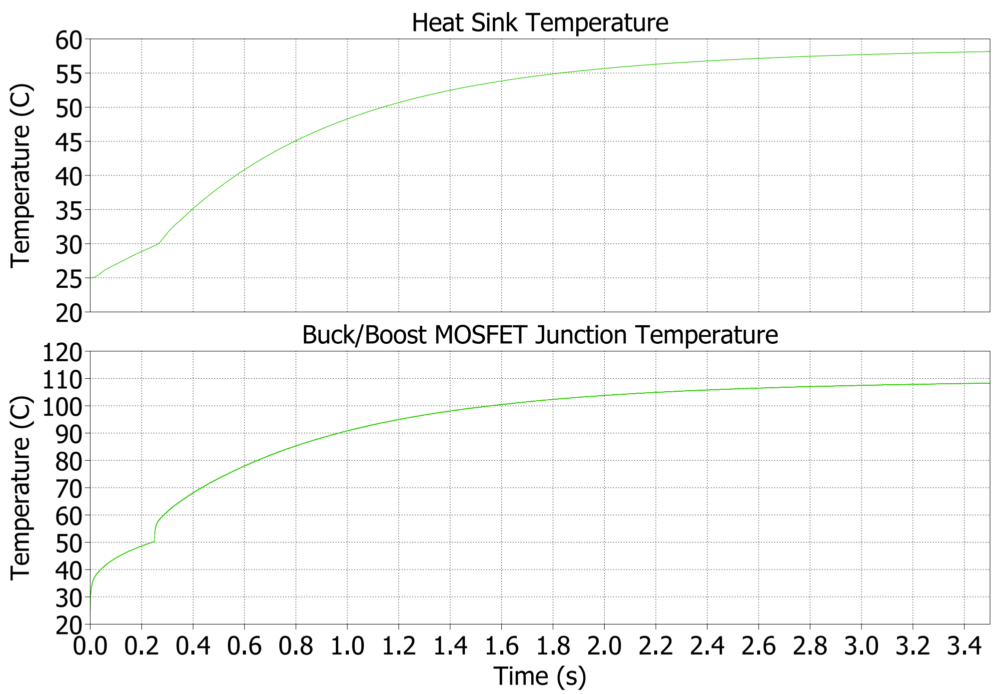

Figure 3.13: Heat sink and buck or boost MOSFET junction temperature while charging a 350 V vehicle at 20 A

One aspect of the thermal analysis that can cause an issue is while running in V2G mode is that to send a full 8 kW to the grid with a lower battery voltage, excessive current is required. For example, a 48 V vehicle would require over 160 A. This is not only above the rated value, but it also can potentially cause damage to the system from thermal mismanagement.

3.4 Charging Results

When examining performance of the charger, there are a number of waveforms that will be analyzed. The first and most important is how well the charger is charging the battery. Battery voltage and current plots will show that the target values are being met. Secondly, grid voltages and currents need to be conditioned by the PFC phase to boost PF. Finally, intermediate voltages and currents will be shown to prove that the various ripple voltages and currents are met.

Throughout each test, the efficiency of the chargers will be presented. As previously mentioned, this value is calculated based only on the power losses within the MOSFETs and their diodes. It has also been mentioned that due to the physical size of the system and time it would typically take for this system to reach a steady state temperature, the efficiency presented is found at a lower temperature than the steady state value. As shown previously, thermal calculations have been done but further testing need to be conducted to establish an actual steady state temperature would be with a purpose built heat sink.

The 350 V vehicle will be examined first as it is the highest power of all the vehicles. To calculate the value of the capacitor in the SOC section of the battery model, Equation 3.8 is used.

$$
\begin{aligned}
C &= 3600 \cdot \text{Capacity} \cdot 2.778 \times 10^{-7} \\
&= 3600 \cdot \frac{100000}{390} \cdot 2.778 \times 10^{-7} = 0.2563\ \frac{\text{kWhr}}{V^2}
\end{aligned}
$$

This value in Farads will be large and will take much longer to show any significant change in SOC within a time frame that PLECS can reasonably show and so it will be divided by 3,000 to show the SOC changing within a short time window. The battery will be set to 30% SOC. A step current input beginning with 10 A and moving to 20 A will be applied.

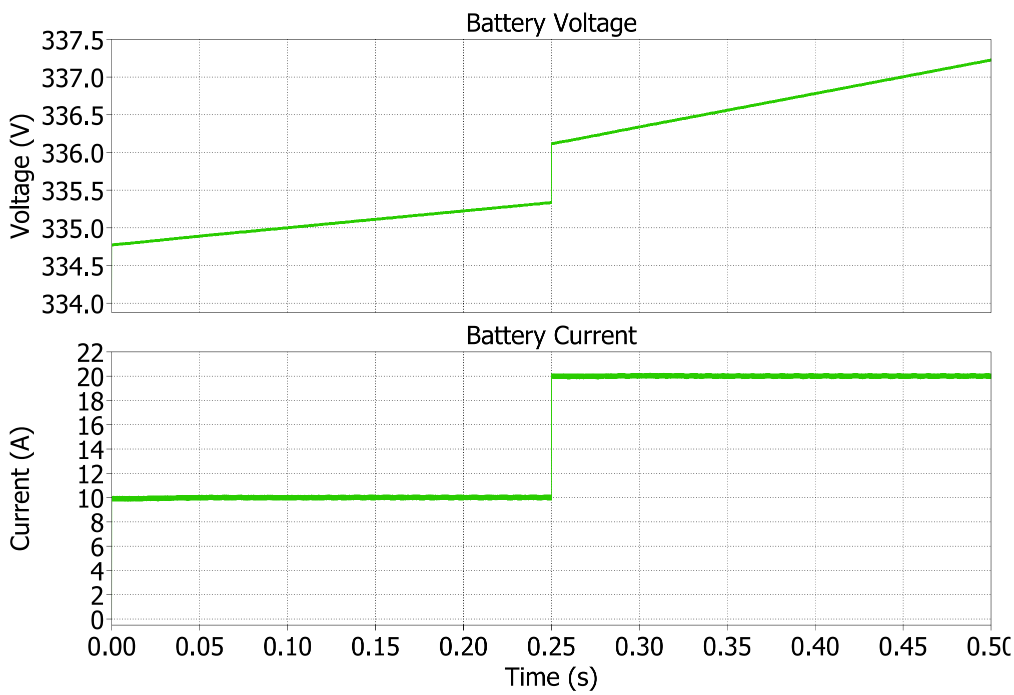

Figure 3.14: Battery voltage and current for the charging of the 350 V vehicle

It can be seen that the charger tracks the desired output correctly and adjusts to the step change in current quickly and without significant transients. A view of this transient and steady state ripple current with a smaller time step is shown in

Figure 3.15.

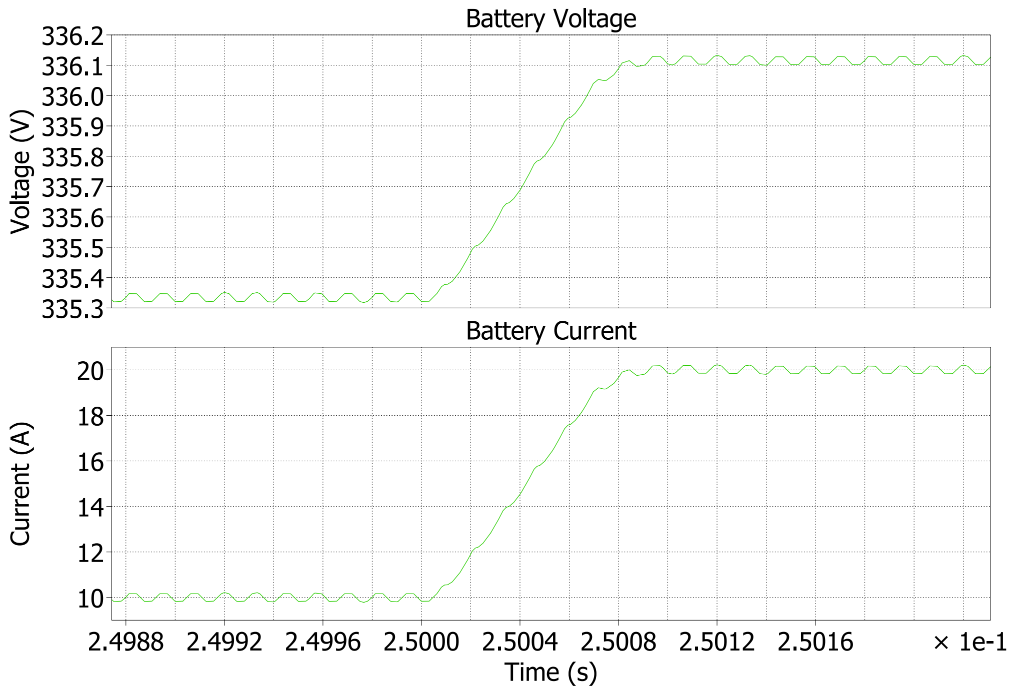

Figure 3.15: Transient and ripple of battery voltage and current for the charging of the 350 V vehicle

Figure 3.15 shows that the current controller is able to ramp the current up at a quick rate while at the same time not having a significant amount of overshoot or ringing that could lead to damage of the battery. It also shows that there is little to no steady state error after only a few switching cycles of the converter. It can also be seen that the voltage and current ripple requirements as defined in Table 3.1 of the converter are easily being met. During the charging time, the charger is running at an efficiency of around 95.7%.

Now that the battery output has been shown, the grid currents and voltages will be analyzed as shown in Figure 3.16. Here the effects of the PFC stage can be seen. The voltage and current are perfectly in phase. The current does have some high frequency ripple which is a result of the PFC switches but despite this noise, the THD is only 0.065 or a PF of 0.998. It can also be seen that there are increases in input current during load transients. When the system initially starts up, there is an inrush current to charge the capacitors. There is another inrush current when the load steps up from 10 A to 20 A. This is due to the large DC link capacitor discharging more power per cycle and the controller requires a few cycles of the AC waveform to correct for this change.

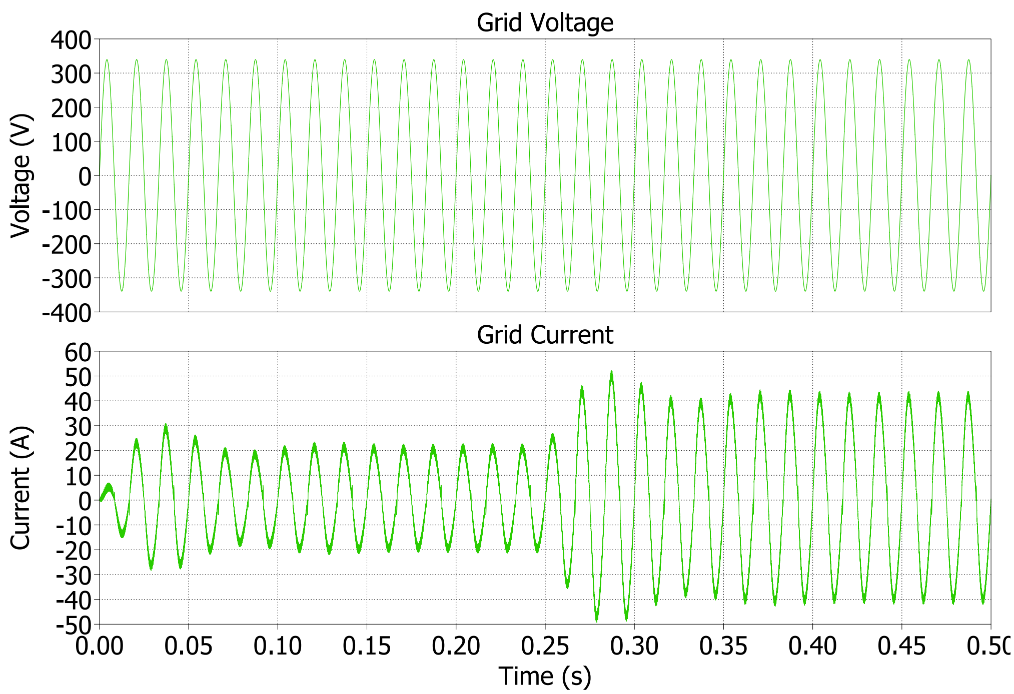

Figure 3.16: Grid voltage and current for the charging of the 350 V vehicle

Each of the inductors in the system are required to be the largest when charging the 350 V vehicle. Figure 3.17 shows the current ripple in the inductor of the buck converter section while running at 20 A. It can be seen that the specification of 10% ripple is met. Figure 3.18 shows the max PFC inductor ripple also meets its given specification of 5%.

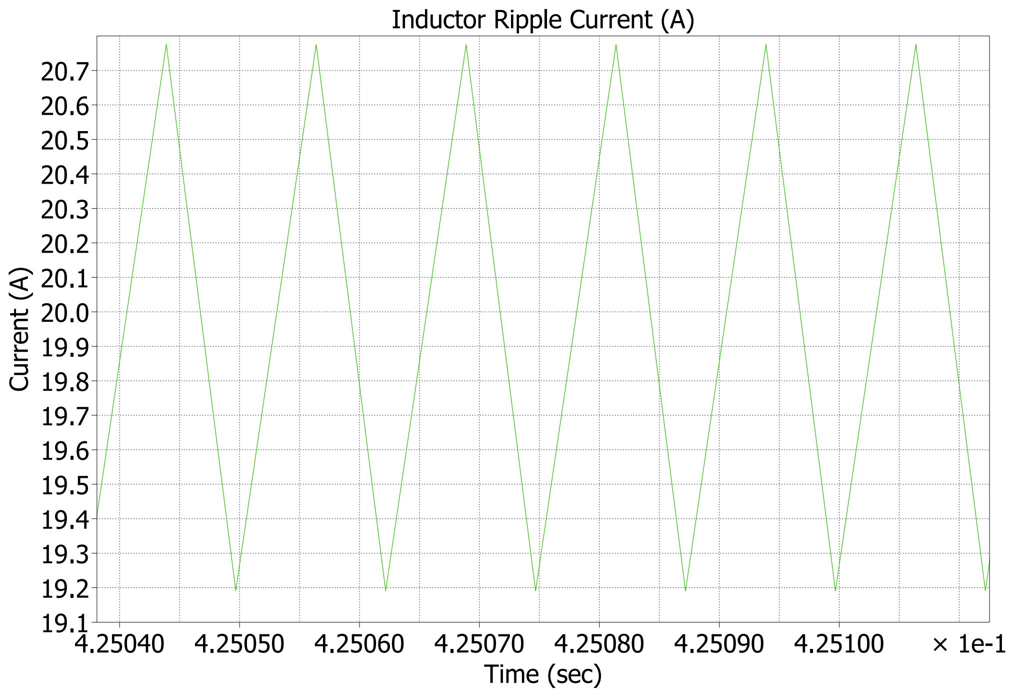

Figure 3.17: Current ripple of the inductor within the buck stage while charging a 350 V vehicle

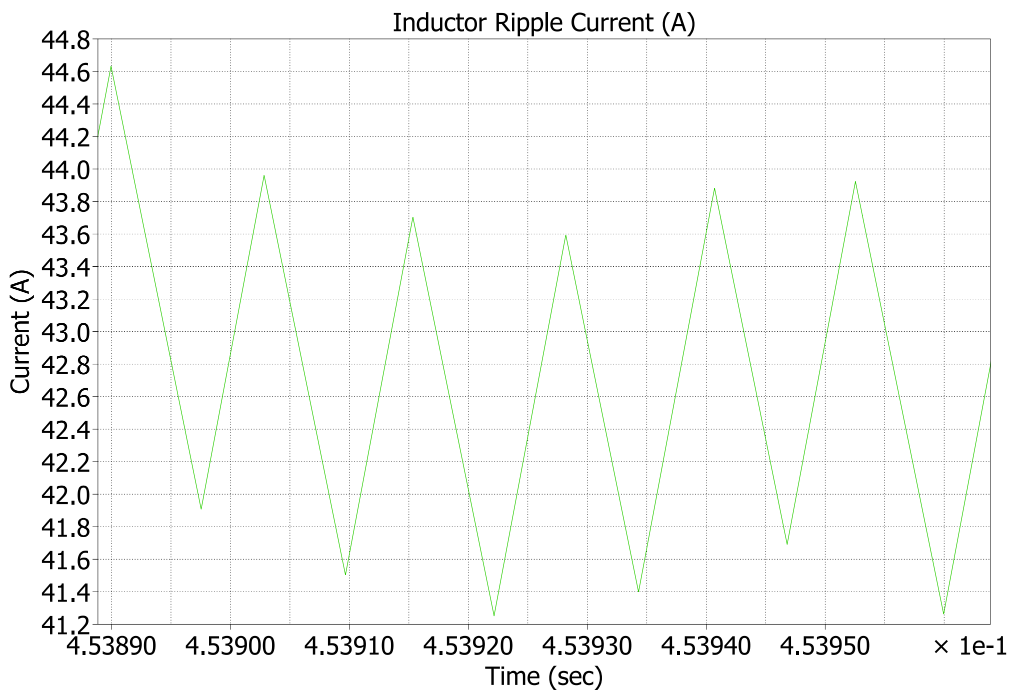

Figure 3.18: Current ripple of the inductor within the PFC stage while charging a 350 V vehicle

The 96 V vehicle will be now be charged. The same step input of 10 A to 20 A will be applied, the battery voltage will be start once again at 30% SOC and the capacity of the battery will be reduced to show the charging battery within the feasible time frame.

Charging waveforms are presented first. Figure 3.19 shows the output voltage and current to the battery. It can be seen that there is some steady state error on start up that is quickly accounted for. While at max power, the charger reaches efficiencies of around 96.2%.

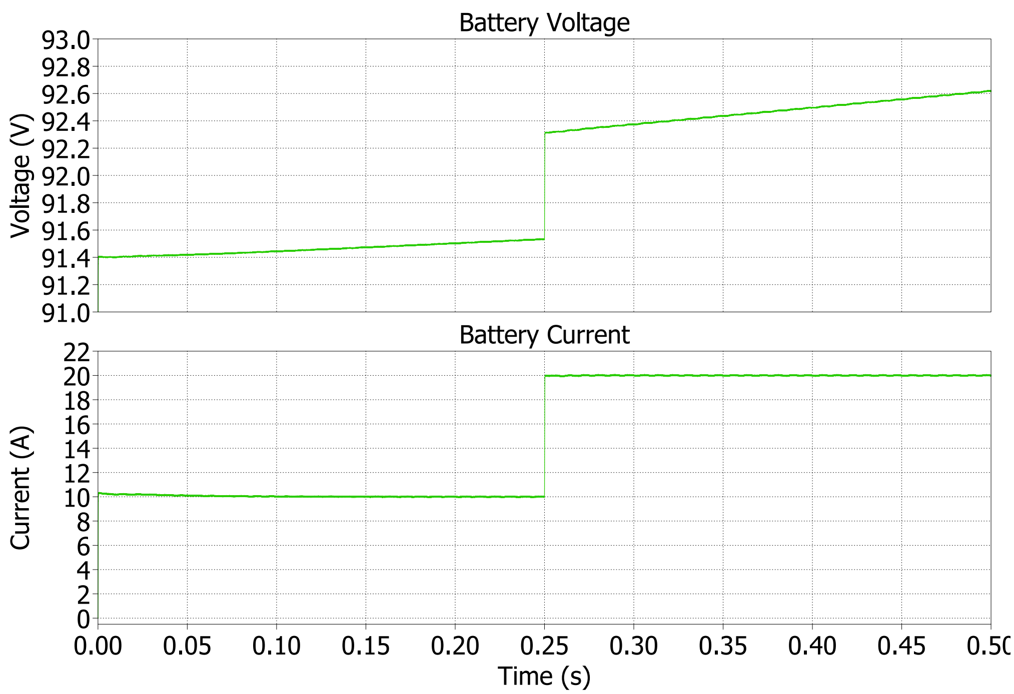

Figure 3.19: Battery voltage and current while charging a 96 V vehicle

Next, Figure 3.20 shows the AC input waveform while charging a 96 V battery. The biggest difference between this waveform and the input voltage and current from charging the 350 V battery (Figure 3.16) is the input current. It is clearly less sinusoidal which results in more THD. For this specific example, the THD while running at the max current is 0.128. This results in a PF of 0.991 which is still high compared to a system without PFC.

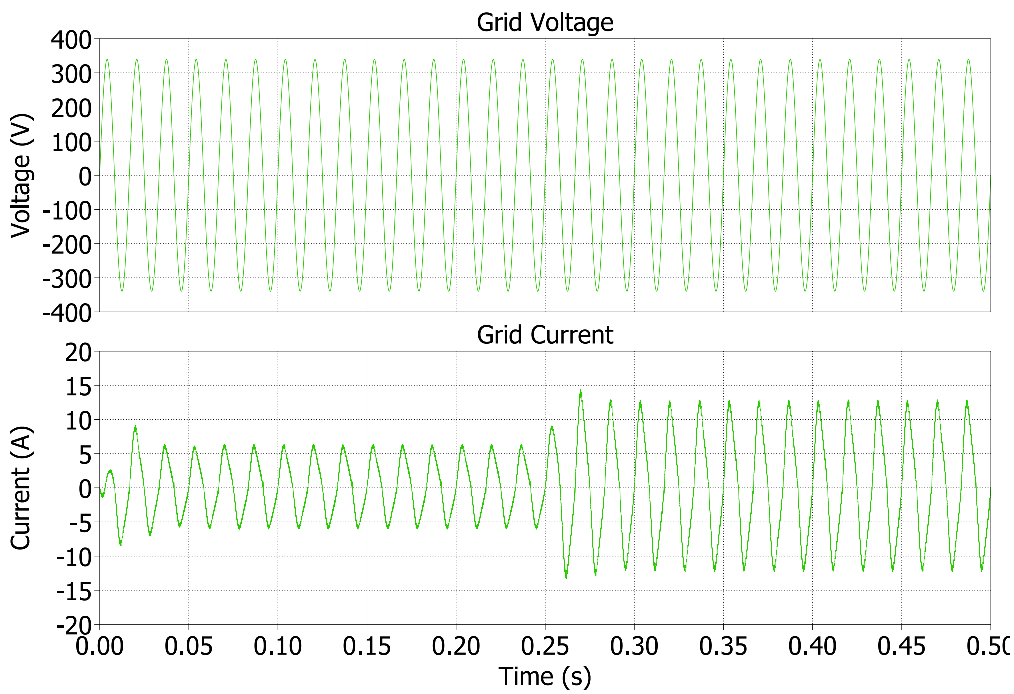

Figure 3.20: Grid voltage and current to the charger while charging a 96 V vehicle

Finally, the 48 V battery will be charged. Similar to the vehicles above, there will be the same step input of 10 A to 20 A, the battery will be set at 30% SOC and the capacity will be reduced to be able to see meaningful change as time progresses.

First, the output to the 48 V battery will be examined. Figure 3.21 shows how the current tracks the set point with minimal overshoot and steady state error. The voltage increases as the pack voltage increases in order to maintain the battery current. The efficiency of the charger in this case is around 95%.

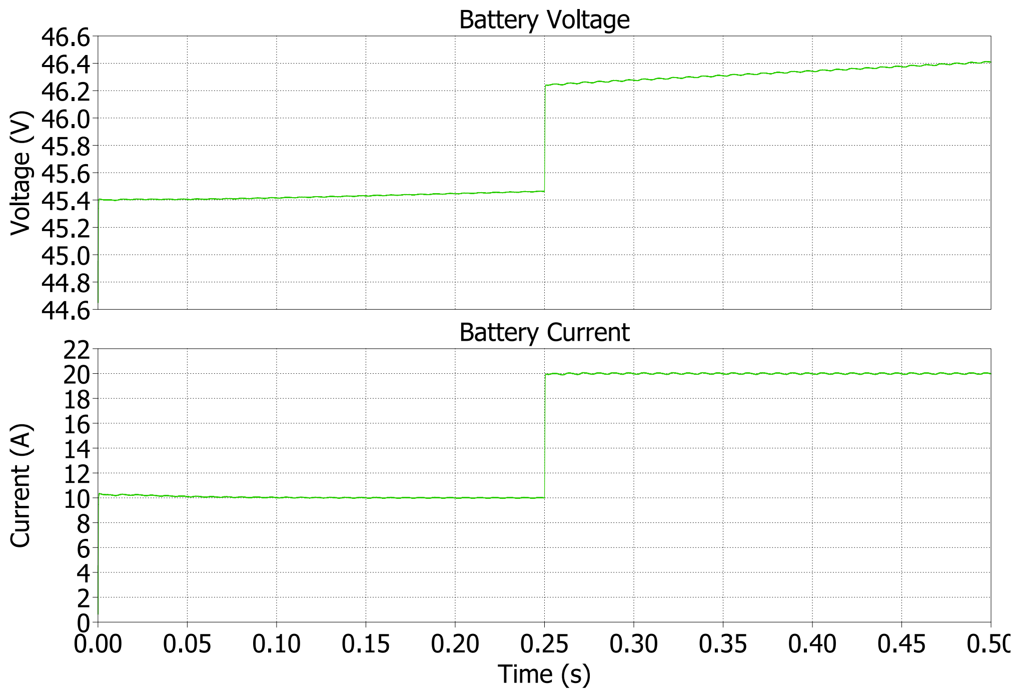

Figure 3.21: Battery voltage and current to the battery while charging a 48 V vehicle

The grid waveforms are more interesting. As the grid current falls, it becomes harder for the PFC to construct a clean sinusoid and thus distortion becomes more of a factor. Despite a THD of 0.3, the PF still remains high due to the two signals remaining in near perfect phase. The PF is still around 0.957 which is acceptable.

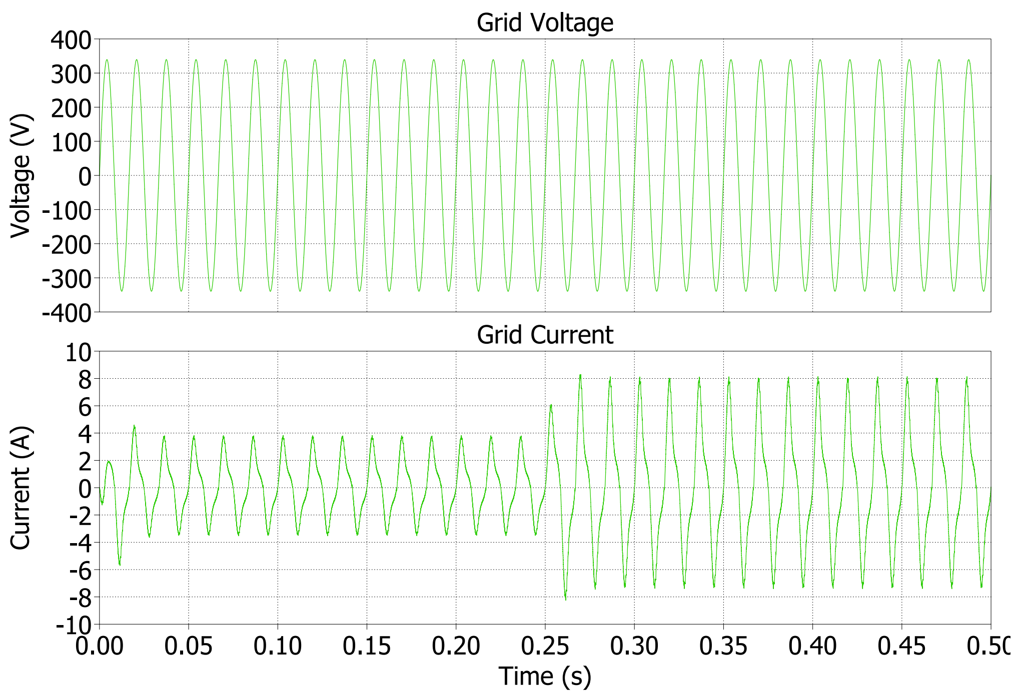

Figure 3.22: Grid voltage and current to the charger while charging a 48 V vehicle

Finally, the DC link capacitor and output buck capacitor are required to be the largest when charging a 48 V battery. Figure 3.23 shows the voltage over the DC link capacitor. The voltage set point is at 100 V. The predominant ripple frequency is at 120 Hz or the second harmonic of the grid frequency. The DC link capacitor is required to be large to filter this out. It can also be seen that the ripple easily matches the specification of 10% ripple and is actually closer to 4%. This significant difference in calculated and experimental ripples could be attributed to the filtering effects of other components within the circuit.

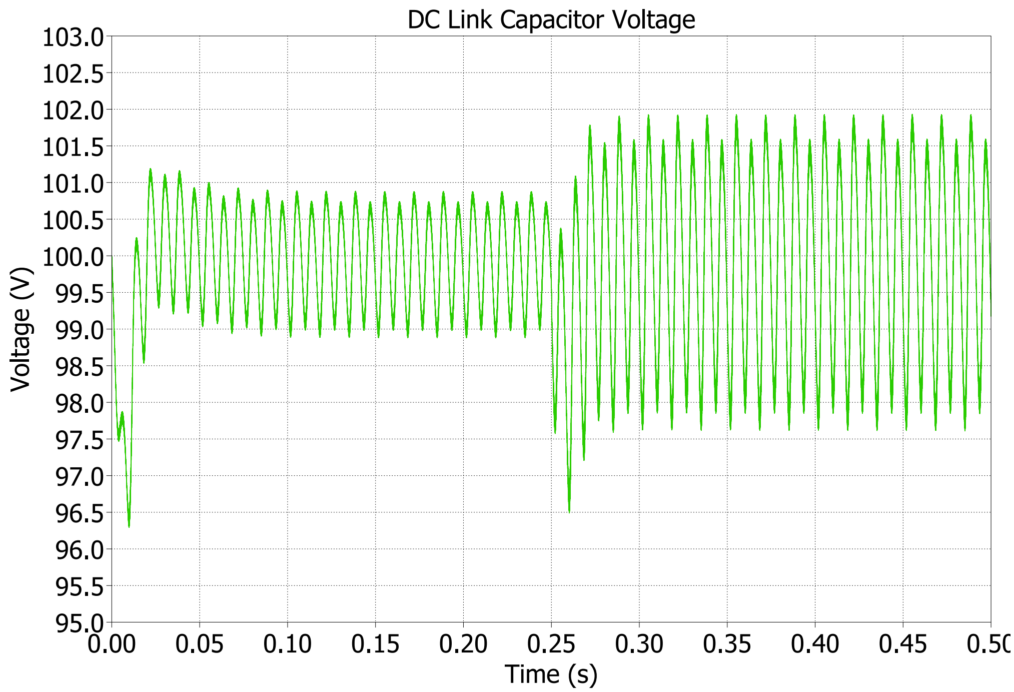

Figure 3.23: Voltage over the DC link capacitor while charging a 48 V vehicle

Figure 3.24 shows the experimental voltage ripple over the output capacitor. Here, the noise at the switching frequency created by the buck converter MOSFET is filtered out and meets the voltage ripple requirement of 5%. Figure 3.21 shows this capacitor voltage ripple in detail.

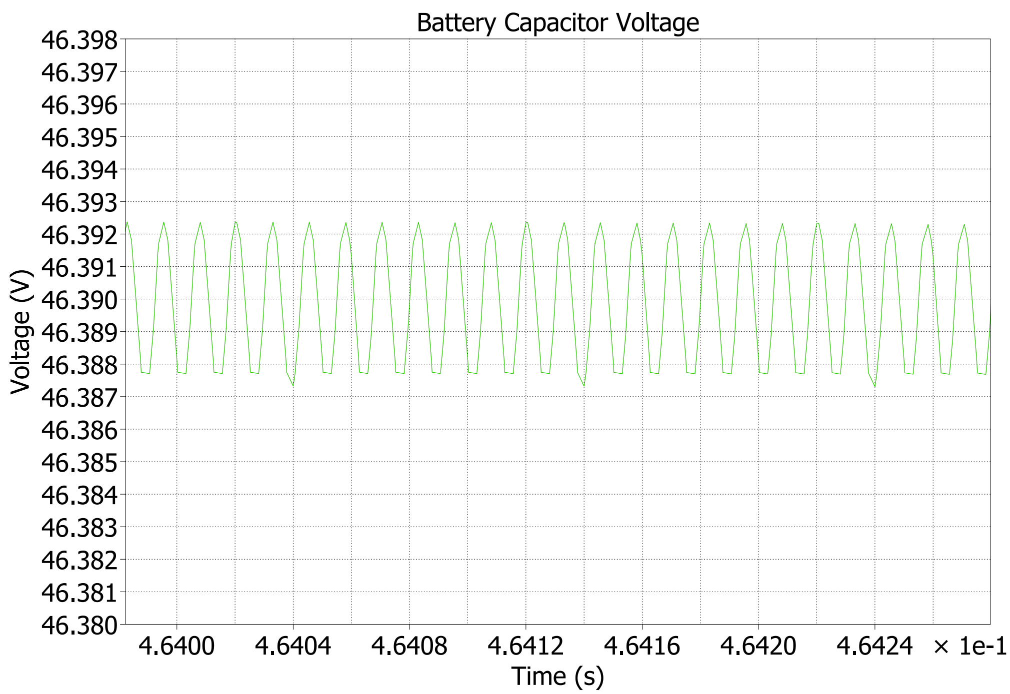

Figure 3.24: Voltage over the battery capacitor while charging a 48 V vehicle

3.5 Vehicle to Grid Results

While in V2G mode, the charger works to take energy from the battery and injects it back into the grid. This mode of operation will be examined in all 3 battery configurations by the way of examining the input and output waveforms. Intermediate waveforms will be analyzed for the 350 V vehicle to show operation is as expected.

To begin, the 350 V vehicle is plugged in. SOC starts at 80%, the capacity is once again reduced, and a constant current of 32 A peak or about 22.6 A RMS will be set to the grid.

Most importantly, the output of the system to the grid is shown in Figure 3.25. Here it can be seen that the voltage and current are in phase with each other. The current appears to be negative because of the polarity of the ammeter. Power being sent to the grid is negative in this case. In the case of the 350 V vehicle, the THD is only 0.066 or a PF of 0.998. It should also be noted that the time to steady state operation is extremely quick at only a few cycles. This system also has a high efficiency of around 96.7%.

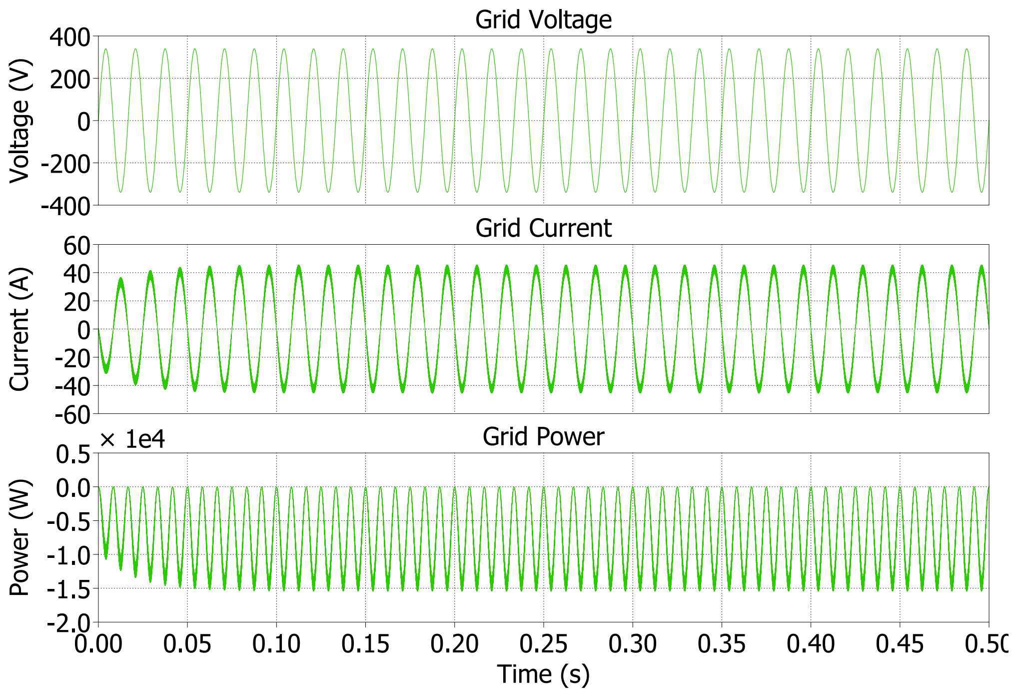

Figure 3.25: Voltage, current, and power being sent to the grid from the 350 V vehicle in V2G mode

Next, the waveforms coming from the battery are examined. Looking at the first cycle of the current, it is seen that there is a large inrush current due to the boost converter starting off at a 50% duty cycle before the controller can correct itself. This doubles the voltage and creates the large inrush current at the large DC link capacitor. The flat section in the current plot represents how the DC link capacitor is discharging to the correct voltage. This inrush current would be eliminated with a more advanced initialization scheme. Next, it can be seen that there is some ringing due to the controller that occurs before reaching a steady state operation around 0.4 seconds.

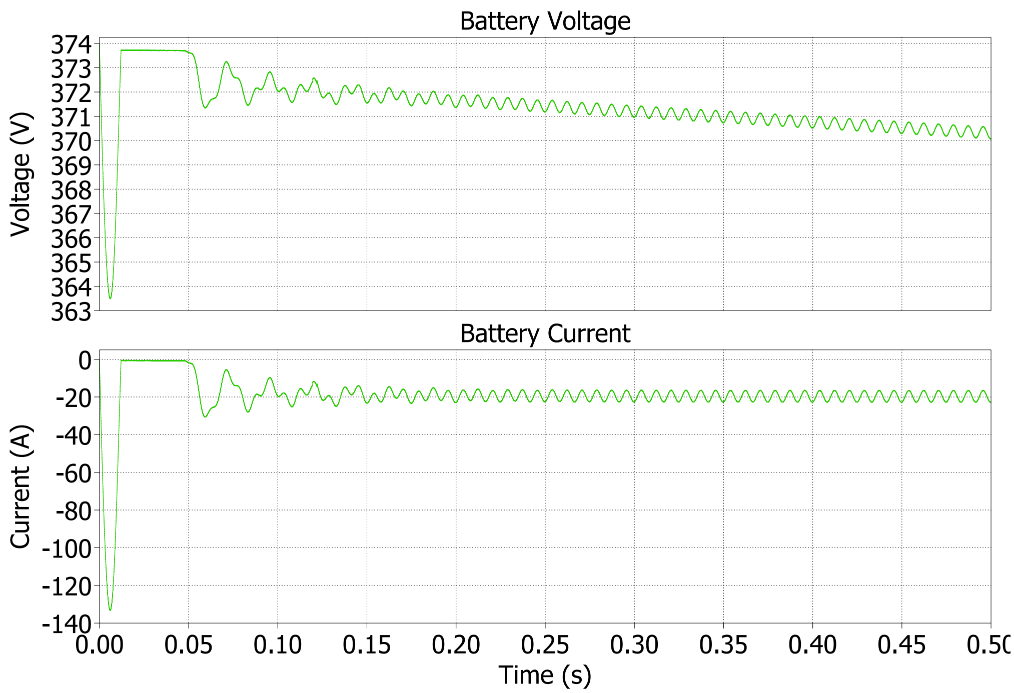

Figure 3.26: Voltage and current from the 350 V vehicle in V2G mode

The DC link capacitor voltage is an important component as it is the link between the boost converter and the inverter stages. Figure 3.27 shows the voltage of this capacitor. As previously mentioned, it can be seen that the voltage spikes up high due to the boost converter running at 50% initially and causing the inrush current. This voltage decreases back below the set point where the controller begins to regulate the duty cycle of the boost converter. The DC link capacitor reaches a steady state near 0.4 seconds into operation.

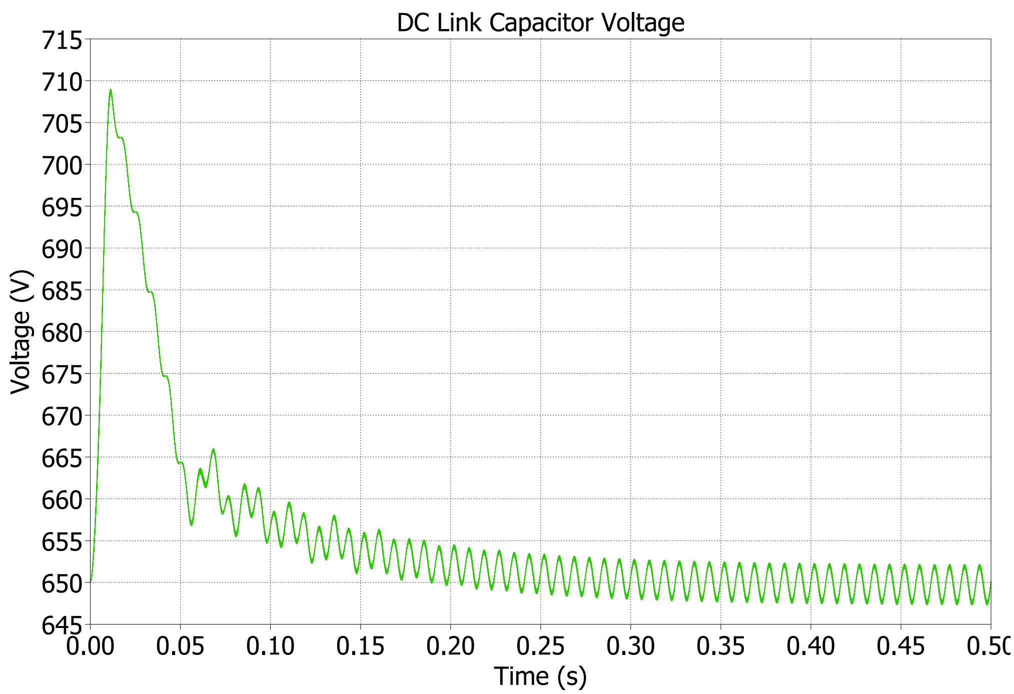

Figure 3.27: Voltage of the DC link capacitor during V2G mode while a 350 V vehicle is plugged in

Moving onto the 96 V vehicle, Figure 3.28 shows the output to the grid. The current plot looks to be a clean sinusoid and the PF of near 1 confirms this. A drawback to this mode is the effect it has on the battery due to the amount of current. This is shown in Figure 3.29. Because of the lower battery voltage and same power demand as the 350 V battery, additional current must be pulled from the battery to meet this demand. Not only does the steady state run at near 60 A, it can reach near 100 A during transient events. This can be problematic due to the MOSFETs within the buck or boost stage only be rated for 63 A as well as the potential for thermal issues to arise. Either lowering the amount of current passing through these two switches or selecting MOSFETs with higher current ratings are two potential solutions to mitigate this concern. Despite these issues, the charger is able to run at about 95.6% efficiency.

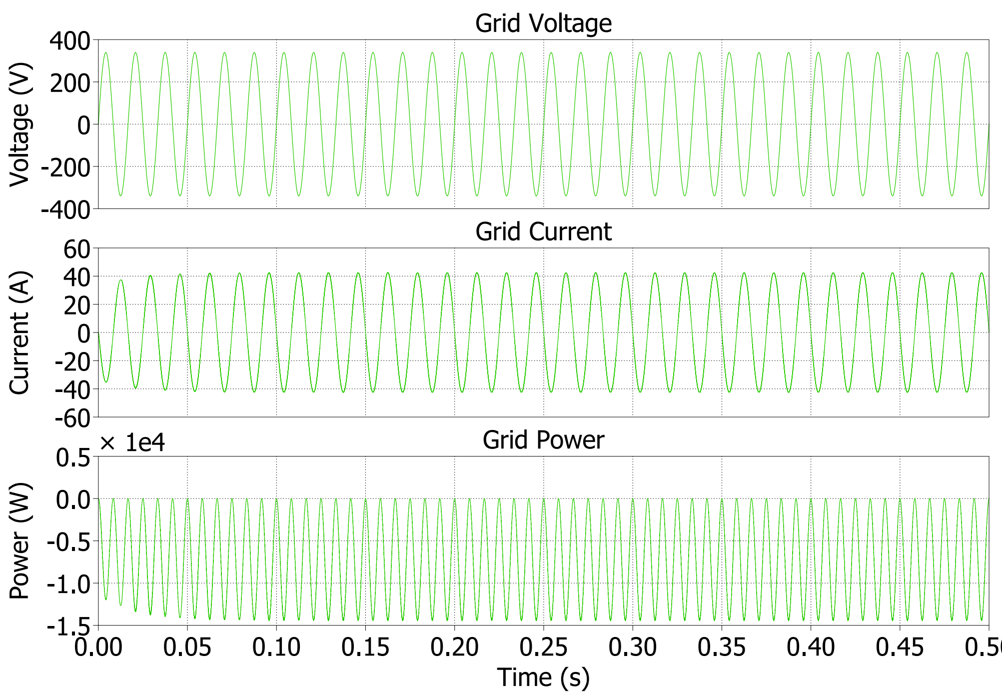

Figure 3.28: Voltage, current, and power being sent to the grid from the 96 V vehicle in V2G mode

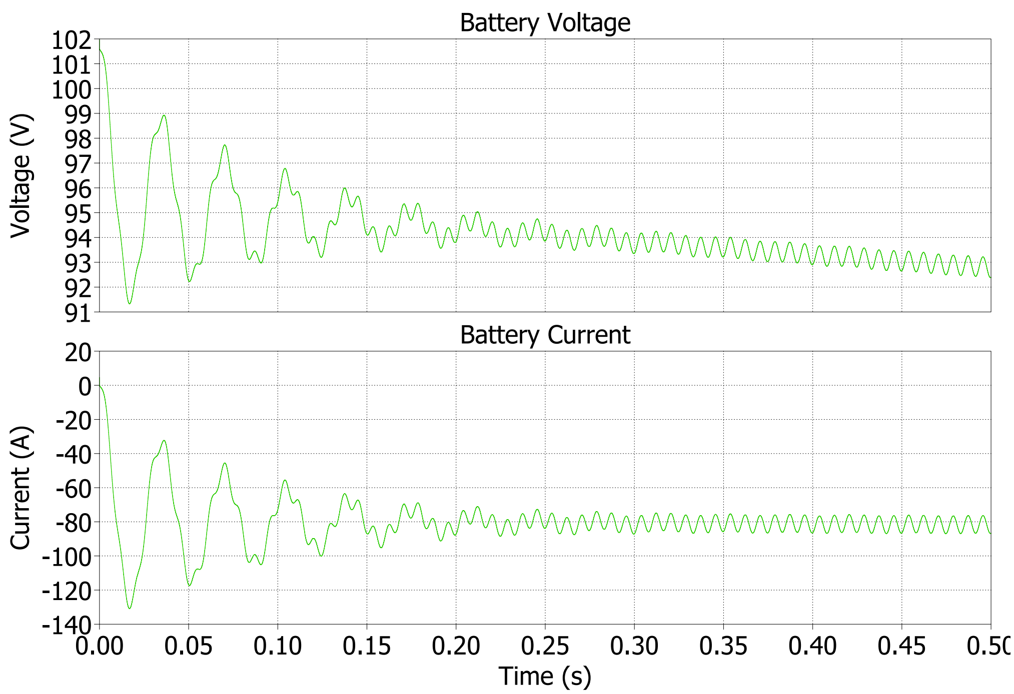

Figure 3.29: Voltage and current from the battery of the 96 V vehicle in V2G mode

As mentioned previously, if the 96 V battery experiences high current problems, so too will the 48 V system. For this test, the current demand will be significantly lowered to explore the effects of sending less than maximum power to the grid. For this test 2 kW will be sent to the grid. This will result in a peak current value of 12 A to the grid.

Initially, the voltage, current, and power waveforms to the grid will be examined. Figure 3.30 shows that the current to the grid has a high PF (1) and minimal THD (.006). Second, the input from the battery is shown in Figure 3.31. Here it can be seen that the input current is less than the input current of the 96 V vehicle at full power. There are also some peaks where the battery current is slightly over 60 A. Despite this, all of the current from the battery is not flowing through the MOSFET which helps with its thermal management. The MOSFETs can also handle peak currents over their rated limit for brief periods but other solutions may need to be considered. One solution to this issue may be that only 350 V vehicles can operate in V2G mode or that the 96 V and 48 V vehicles need to run at a significantly lower output power rating. Despite this high current condition, the charger was able to achieve an efficiency of 94%.

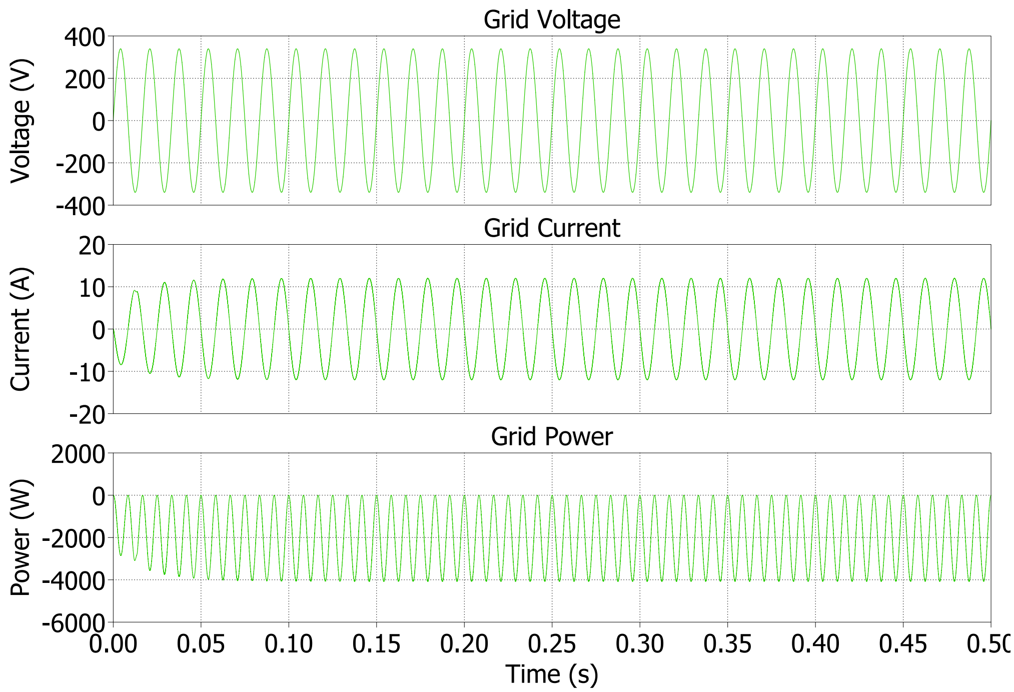

Figure 3.30: Voltage, current, and power being sent to the grid from the 48 V vehicle in V2G mode

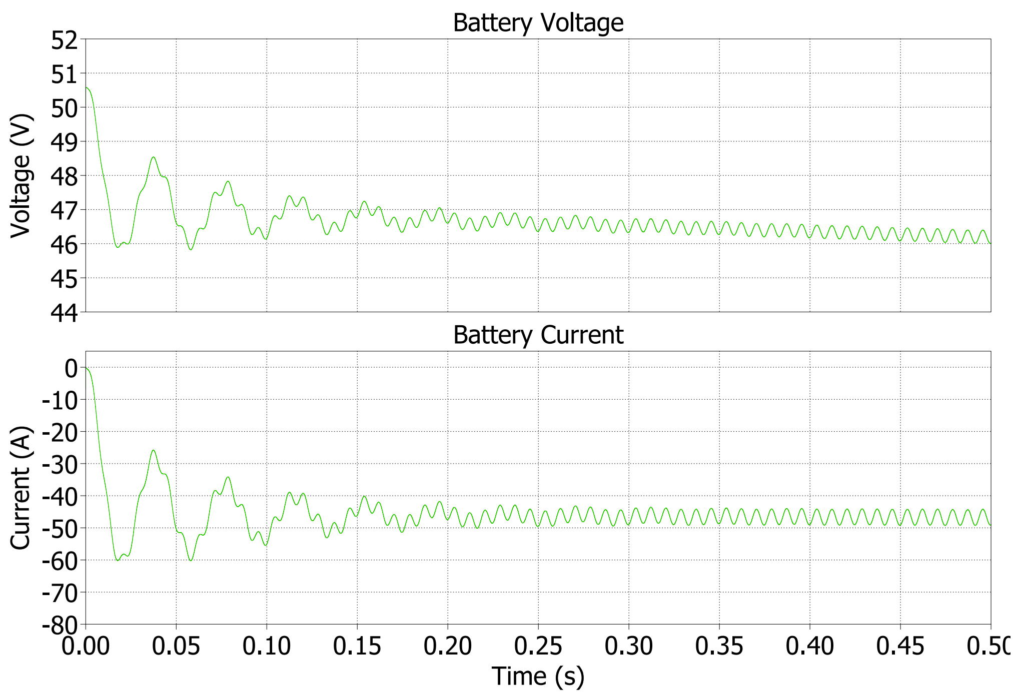

Figure 3.31: Voltage and current from the battery of the 48 V vehicle in V2G mode

One side effect of this circuit that has been neglected in the above results is the inrush current at the beginning of the simulation. This was mitigated by setting the large DC link capacitor and output capacitor near the battery to have initial voltages. This allows for simpler steady state analysis due to the full waveform being viewed more easily. Figure 3.32 shows this inrush current as seen by the grid. Here, the inrush current in the first few cycles can reach over ten times the normal steady state value resulting from the high DC voltage and large capacitance.

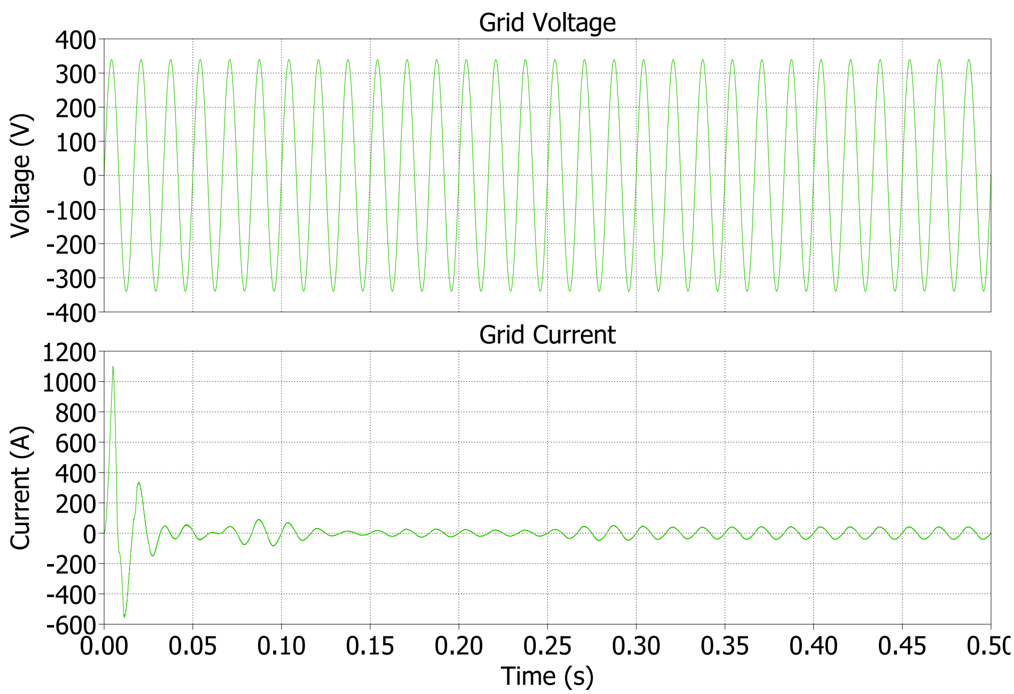

Figure 3.32: Grid voltage and current to the charger while in charging mode with emphasis on the inrush current

As previously mentioned while discussing the sizing of the DC link capacitor, the voltage ripple goal is exceeded by a substantial amount. This signifies that the value of the DC link capacitor could be reduced to limit inrush current while still meeting voltage ripple targets. Figure 3.33 shows the input current if the capacitor was reduced down to 3.8 mF. With this change, the inrush current becomes nearly three times less than with the larger capacitors.

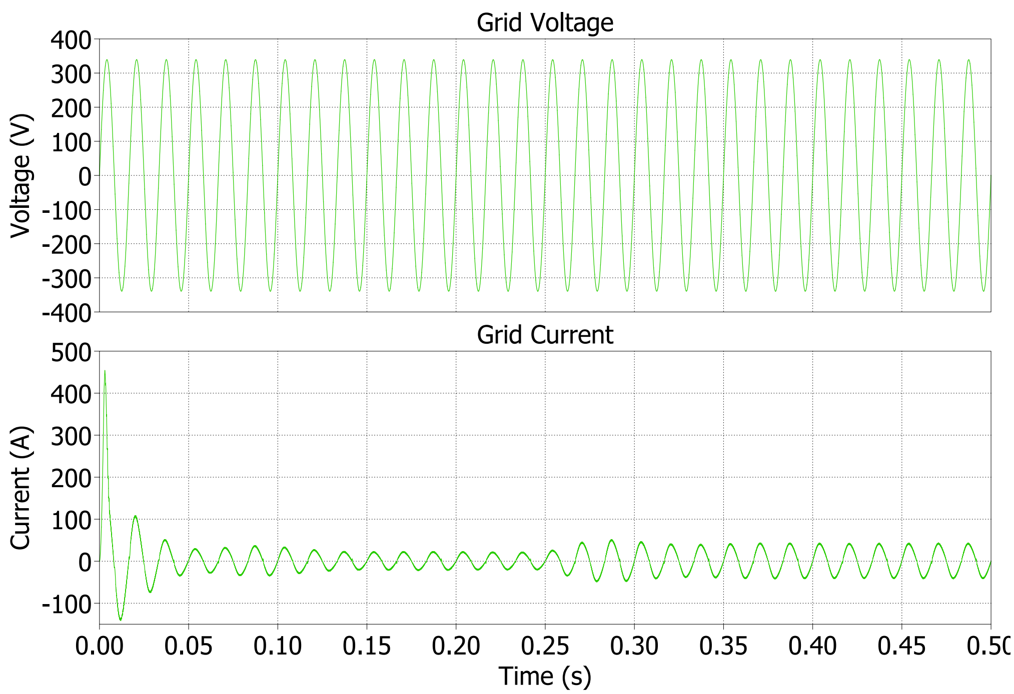

Figure 3.33: Grid voltage and current to the charger while in charging mode with a reduced DC link capacitor value with emphasis on the inrush current

Despite the inrush current decreasing, a capacitor precharge stage or larger MOSFETs should still be considered to mitigate this danger. It should also be noted that within a real circuit, there will also be more parasitic resistances which would also help to reduce this inrush. Another option is to have a soft start feature. This section of code would run only when the capacitors were discharged. The voltage over them would be ramped up which would reduce the amount of inrush current because they would start at lower voltages.

Figure 3.34 shows the DC link capacitor voltage while it is charging a 48 V vehicle. This is the worst case condition to ensure the goal of 10% ripple is still met with the reduced capacitance.

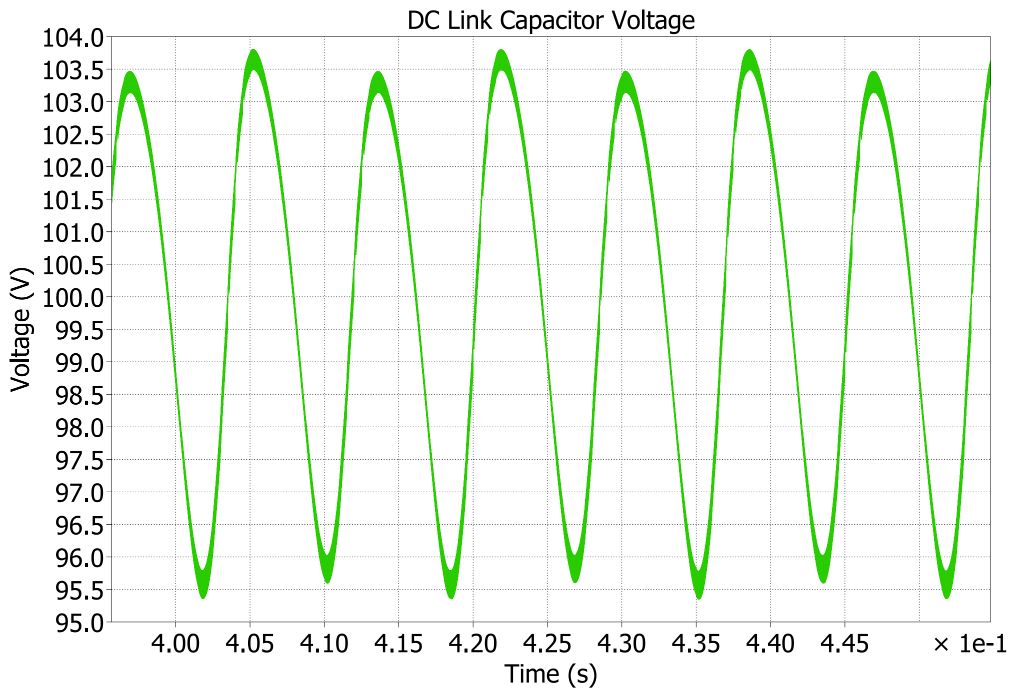

Figure 3.34: DC link capacitor voltage with a reduced DC link capacitor value

3.6 Future Work and Conclusion

Looking forward to the next steps and continuation of this project, there are a number of steps that could be done with the final goal of having a working prototype. These goals would include additional simulations, part specification, assembly, and validation.

Additional simulations would include a program to better analyze the thermal attributes of the circuit. A simulation that would run quicker and for longer periods of time would be needed to get an accurate view of the type of heat sink required as it would need to be a purpose built unit. The controls of the circuit would need to be programmed into a usable microcontroller which would interact with the components in the circuit. This code would need to be implemented and tested with hardware not included in this proposed charger. This includes gate drives and voltage or current protection devices.

Secondly, additional part specification would need to be done. To have a working prototype, each part to be used would need to be found and ordered. This would include the sections of the circuit that are not included including gate drives, snubber devices, microcontrollers, connectors, wires, cables, and more.

Next, assembly would need to be considered. Complete schematics and printed circuit boards (PCBs) would need to be developed and manufactured and parts would need to be placed on boards.

Finally, validation would need to be done to ensure that the charger is operating correctly. To accomplish this, each intermediate step would need to tested to confirm normal operation. The largest portion of this would include testing of the gate drive circuits and their response at various load powers. To perform system validation, a number of safety features would also need to be in place both on the AC and the battery side to ensure safe operation if an unexpected condition arose.

While developing the purpose built off-board charger, a number of challenges arose from limitations or effects of using PLECS as well as design challenges that came from creating this circuit. As mentioned previously, PLECS is not an ideal program for thermal simulations of larger systems due to the inherently large thermal capacitance. To simulate the system using realistic values, a long simulation time would be required which results in long run times of the program. Another area of the circuit that gets limited by runtime is how the SOC is tracked. If the simulation is run for a short enough period to analyze the small signals, there is not enough time for have a significant change in the SOC. As mentioned above, this is remedied by reducing the value of the capacitor to reduce the capacity of the battery thus allowing for the user to see changes in SOC in short periods of time.

Some challenges that were discovered due to the circuit itself included the inrush currents and V2G power requirements. Each of these issues could have been seen while designing the system but were overlooked. As mentioned, the inrush current could be mitigated by running code that includes a soft start. The power requirement issue in V2G mode arises when a lower voltage vehicle is required to provide the max power of 8 kW to the grid. This results in excessive current being drawn from the battery and such through some of the MOSFETs which would need to be considered in the thermal analysis and for the characteristics of each of the MOSFETs.

This paper shows a unique design for an off-board purpose built battery charger. This battery charger was designed to meet the goal of charging various types of vehicles and due to the multi-tap transformer, it is always able to run at similar operating points. The paper then shows how each stage could be implemented and how each one would interact. The proposed charger is then simulated using a PLECS model to show that the input, output, and intermediate steps all follow the expected waveforms of such a system. The paper concludes by describing the next step one would need to take to further validate the design and eventually test in the field.

Chapter 4: Conclusion

The journey toward electrification in the aviation industry has been a topic for many years now. The largest focus of this electrification has been on the aircraft themselves but in today's world, a more realistic application of an electrified airport is on the ground. The ground support vehicles are a good place to begin to implement these ideas.

The biggest change to the way these vehicles would service the planes would be in how they are charged. With fossil fuel vehicles, the gas tanks are simply filled and they are dispatched to the next plane. Electric vehicles take time to charge. Because of this, the electric vehicles need to be scheduled intelligently. This includes when they are both in service and being charged. Manuscript 1 (Charging Analysis of Ground Support Vehicles in an Electrified Airport) shows a potential method of scheduling these vehicles. It also shows how the cost of the system could be minimized depending on the specific needs of an airport. The paper concludes with specific points of interest and why each one is a possible solution.

Not only do these vehicles need to be scheduled intelligently, they need to charge efficiently and inexpensively for the move to electric vehicles to make financial sense. One way to make the ground support vehicles cheaper is to remove the chargers from them and use an off-board one. A sample charger is proposed in

Manuscript 2 (Analysis of a Purpose Built Charger for Ground Support Vehicles in an Electrified Airport). This allows for less weight and complexity as well as eliminating an expensive component by using a purpose built off-board charger. As presented above, this charger is able to run efficiently at similar set points while at the same time charging a wide range of vehicles and maintaining a high efficiency.

Within both of the presented manuscripts, and particularly the first, the overall cost of the system is a variable that has been designed for. With the end goal being that the proposed charger would be used in the electrified airport model, a total cost of the charger would need to be found and implemented into the simulations to verify that it would make financial sense to use such a device. This total cost could be used within Manuscript 1 to get a better estimate of what price it would cost to run each set of parameters as well as help in finding a maximum “goal” cost that could be spent on the charger to make the construction of it feasible.

The two manuscripts provided show a comprehensive approach to how a fleet of ground support vehicles within an electrified airport could be implemented. It discusses how many vehicles would be needed given a set of constraints, how this system would be optimized, how the vehicles would be scheduled to be used and charged, and finally, how a component level charger could be used to efficiently charge various types of vehicles.

Bibliography

[1] M. D. Moore, “Misconceptions of electric aircraft and their emerging aviation markets,” 52nd Aerospace Sciences Meeting, Oct. 2014.

[2] B. Sarlioglu and C. T. Morris, “More electric aircraft: review, challenges, and ppportunities for commercial transport aircraft,” IEEE Transactions on Transportation Electrification, vol. 1, no. 1, pp. 54-64, June 2015.

[3] “U.S. national electrification assessment,” Electric Power Research Institute, rep., Apr. 2018.

[4] K. Gulan, E. Cotilla-Sanchez, and Y. Cao, “Charging analysis of ground support cehicles in an electrified airport”, in Proceedings of 2019 IEEE Transportation Electrification Conference and Expo (ITEC), in press, Novi, MI, 2019.

[5] W. Su, H. Eichi, W. Zeng and M. Chow, “A survey on the electrification of transportation in a smart grid environment,” IEEE Transactions on Industrial Informatics, vol. 8, no. 1, pp. 1-10, Feb. 2012.

[6] K. J. Dyke, N. Schofield and M. Barnes, “The impact of transport electrification on electrical networks,” IEEE Transactions on Industrial Electronics, vol. 57, no. 12, pp. 3917-3926, Dec. 2010.

[7] A. Hilshey, P. Hines, P. Rezai and J. Dowds, "Estimating the impact of electric vehicle smart charging on distribution transformer aging," Proc. 2013 IEEE Power & Energy Society General Meeting, Vancouver, BC, 2013.

[8] A. D. Hilshey, P. D. H. Hines, P. Rezaei and J. R. Dowds, "Estimating the impact of electric vehicle smart charging on distribution transformer aging," IEEE Transactions on Smart Grid, vol. 4, no. 2, pp. 905-913, June 2013.

[9] Khalil, Ashraf. (2019). "Delay margin computation for load frequency control system with plug-in electric vehicles". International Journal of Power and Energy Systems. January 2019.

[10] M. Wallin, "Monte carlo simulation in statistical physics". Stockholm, Sweden, 2005.

[11] X. Hu, M. Wang and E. Di Paolo, "Calculating complete and exact pareto front for multiobjective optimization: a new deterministic approach for discrete problems," IEEE Transactions on Cybernetics, vol. 43, no. 3, pp. 1088-1101, June 2013.

[12] "Used aircraft ground support equipment/ GSE," Global GSE. [Online]. Available: https://www.globalgse.com/.

[13] K. Morrow, D. Hochard, and J. Francfort, "Cost benefit analysis modeling tool for electric vs. eCE airport ground support equipment development and results", Idaho Falls, Idaho, rep., 2007.

[14] J. Ou, X. Liu, X. Li and X. Shi, "Mapping global fossil fuel combustion CO2 emissions at high resolution by integrating nightlight, population density, and traffic network data," IEEE Journal of Selected Topics in Applied Earth Observations and Remote Sensing, vol. 9, no. 4, pp. 1674-1684, April 2016.

[15] K. D. Edwards, R. M. Wagner, and T. J. Theiss, "Defining engine efficiency limits", October 2011.

[16] X. Yu, C. Cecati, T. Dillon, M. G. Simoes, "The new frontier of smart grids", IEEE Ind. Electron. Mag., vol. 5, no. 3, pp. 49-63, September 2011.

[17] "Model s owner's manual", December 2018. [Online]. Available: https://www.tesla.com/.

[18] B. Halvorson, "Rivian electric pickup, suv ready for future 800v upgrade-possibly in 2022, Green Car Reports, December 21, 2018. [Online]. Available: https://www.greencarreports.com/.

[19] "Tow tractor specifications". [Online]. Available: https://www.taylor-dunn.com.

[20] J. G. Hayes and G. A. Goodarzi, "Electric powertrain energy systems, power electronics & drives for hybrid, electric & fuel cell vehicles". Hoboken, NJ: John Wiley & Sons, 2018.

[21] A. Namboodiri and H. S. Wani, "Unipolar and bipolar pwm inverter", International Journal for Innovative Research in Science & Technology, vol. 1, no. 7, December 2014.

[22] N. Greco, A. Parisi, G. Palmisano, N. Spina and E. Ragonese, "Integrated transformer modelling for galvanically isolated power transfer systems", 2017 13th Conference on Ph.D. Research in Microelectronics and Electronics (PRIME), Giardini Naxos, 2017, pp. 325-328.

[23] Y. Cao, R. C. Kroeze, and P. T. Krein, Multi-timescale parametric electrical battery model for use in dynamic electric vehicle simulations, IEEE Transactions on Transportation Electrification, vol. 2, no. 4, pp. 432-442, 2016.

[24] C. Liu, K. T. Chau, D. Wu and S. Gao, "Opportunities and challenges of vehicle-to-home, vehicle-to-vehicle, and vehicle-to-grid technologies", Proceedings of the IEEE, vol. 101, no. 11, pp. 2409-2427, November 2013.

[25] C. Jin, J. Tang, P. Ghosh, "Optimizing electric vehicle charging with energy storage in the electricity market", IEEE Trans. Smart Grid, vol. 4, no. 1, pp. 311-320, February 2013.

[26] X. Gong and G. Wang, "98.6% efficiency, 6.6-kW totem-pole pfc reference design for hev/ev onboard charger", Aug-2018. [Online]. Available: ti.com.

[27] R. Teodorescu, F. Blaabjerg, M. Liserre and P. C. Loh, "Proportional-resonant controllers and filters for grid-connected voltage-source converters", IEEE Proceedings - Electric Power Applications, vol. 153, no. 5, pp. 750-762, September 2006.

[28] M. Restrepo, J. Morris, M. Kazerani, and C. A. Caizares, Modeling and testing of a bidirectional smart charger for distribution system ev integration, IEEE Transactions on Smart Grid, vol. 9, no.1, January 2018, pp. 152-162.

[29] J. Tucker, "Understanding output voltage limitations of dc/dc buck converters, 2008.

[30] Min Chen and G. A. Rincon-Mora, "Accurate electrical battery model capable of predicting runtime and i-v performance", IEEE Transactions on Energy Conversion, vol. 21, no. 2, pp. 504-511, June 2006.

[31] Y. Cao and P. T. Krein, An average modeling approach for mobile refrigeration hybrid power systems with improved battery simulation, Proc. IEEE Transportation Electrification Conf. (ITEC), 2013, pp. 1-6.

[32] Y. Cao, M. A. Williams, B. J. Kearbey, A. T. Smith, P. T. Krein, and A. G. Alleyne, 20x-real time modeling and simulation of more electric aircraft thermally integrated electrical power systems, Proc. IEEE International Conf. Electrical Systems for Aircraft, Railway, Ship Propulsion and Road Vehicles (ESARS-ITEC), 2016, pp. 1-6.

[33] "Lithium-ion battery data sheet", Ineltro, November 2010.

[34] N. Mohan, "Power electronics: a first course". Hoboken, N.J: Wiley, 2012.

[35] "Body diode characteristics — basic knowledge," ROHM TECH WEB: Technical Information Site of Power Supply Design. [Online]. Available: https://micro.rohm.com/.

[36] “C3M0030090K”. [Online]. Available: https://www.wolfspeed.com/.

[37] “BSM120D12P2C005 datasheet.” [Online]. Available: https://www.rohm.com/

APPENDICES

Appendix A: PLECS Blockset

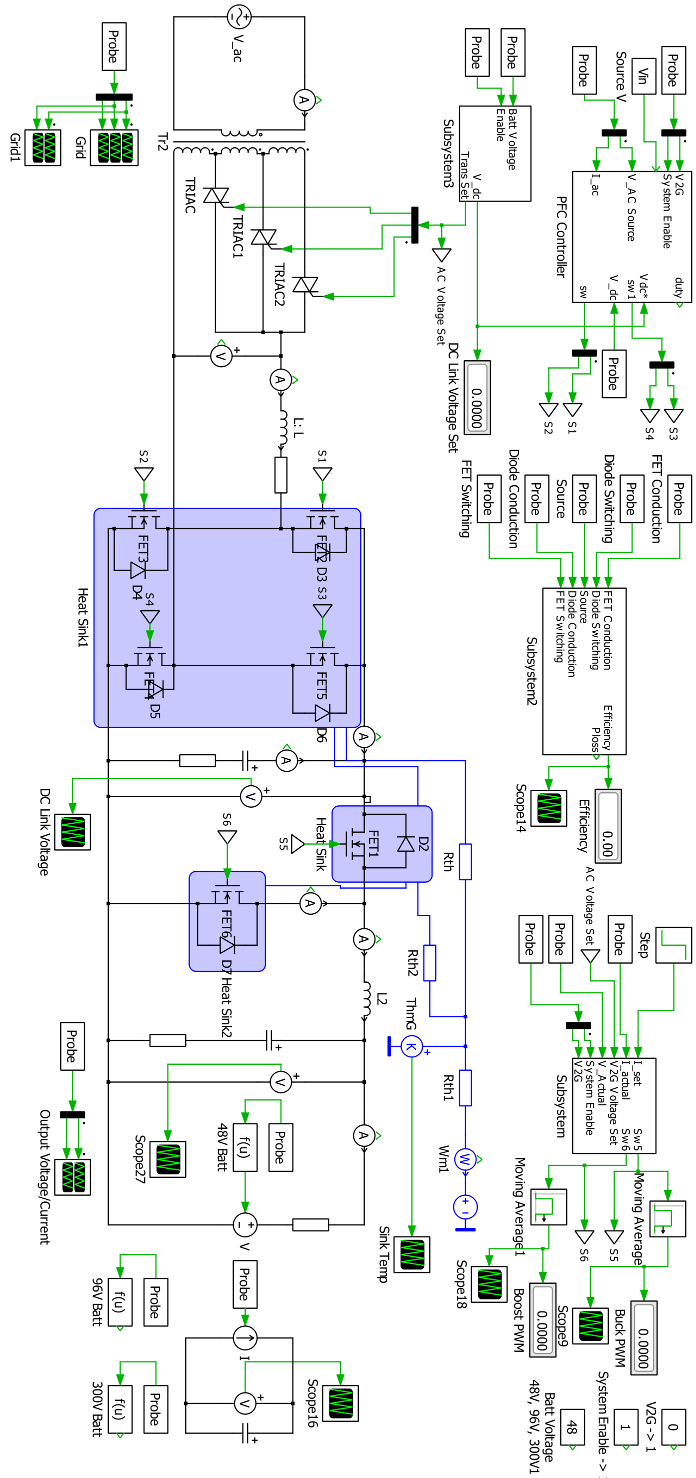

Figure A.1: The proposed charger model as seen in PLECS

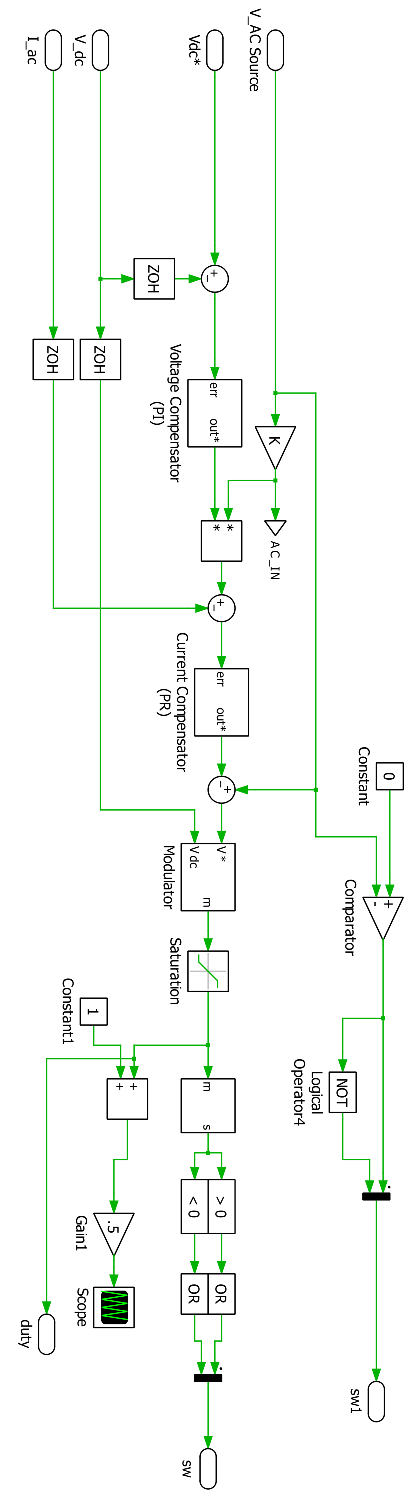

Figure A.2: PFC controls for vehicle charging as seen in PLECS

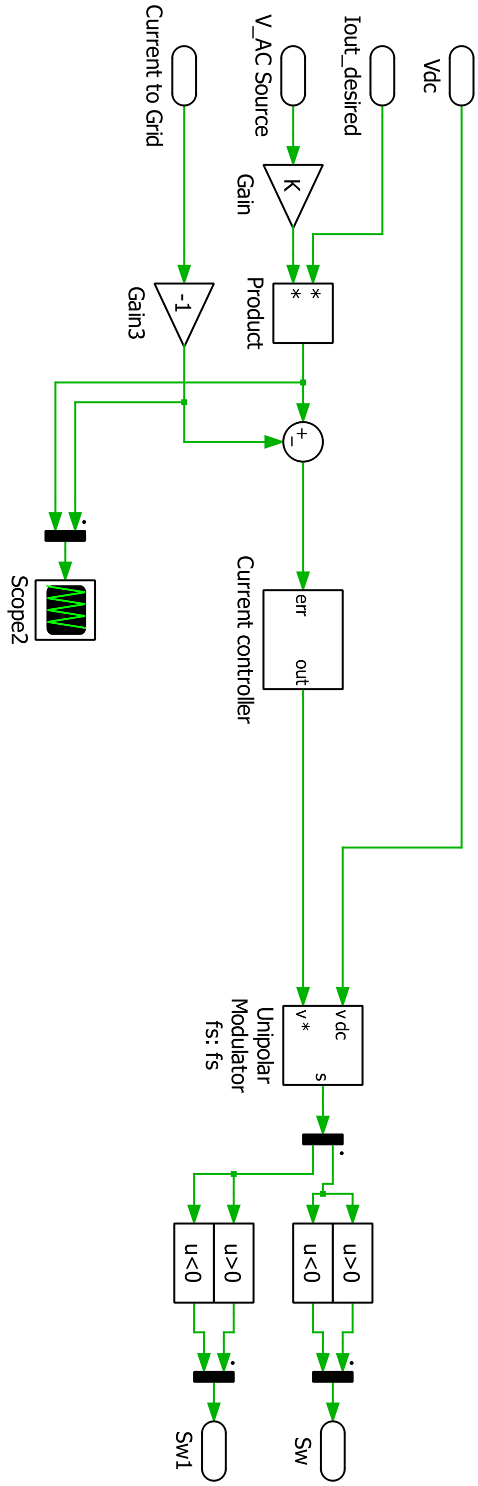

Figure A.3: V2G controls as seen in PLECS

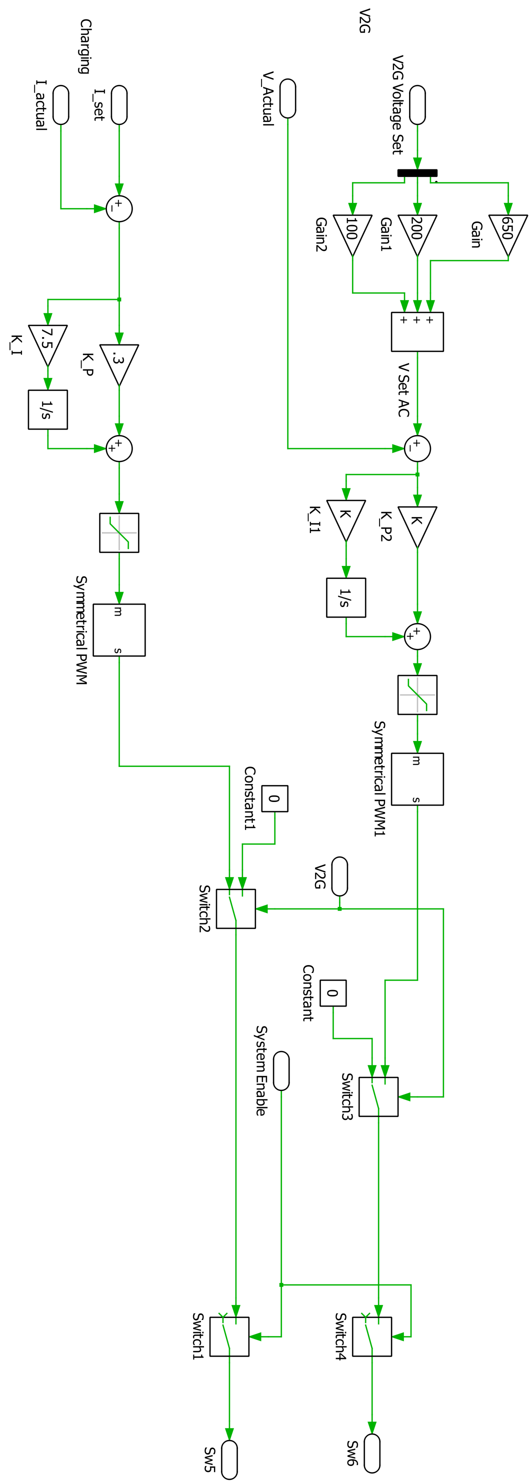

Figure A.4: Buck/boost stage controls as seen in PLECS